

Chapter 3. Nanostructures Technology, Research and Applications

Academic and Research Staff

Professor Henry I. Smith, Dr. David J.D. Carter, Dr. James G. Goodberlet, Dr. Mark L. Schattenburg, James M. Carter, Robert C. Fleming, Mark K. Mondol

Visiting Scientists and Research Affiliates

Dr. Patrick N. Everett, Dr. Jawoong Lee, Ken-Ichi Murooka

Graduate Students

Nitza M. Basoco, David Berman, Aleksandr Bernshteyn, Carl G. Chen, Alexei A. Erchak, Maya S. Farhoud, Juan Ferrera, Darío Gil, Yaowu Hao, Jeffrey T. Hastings, Min-ha Hwang, Keith M. Jackson, M. Jalal Khan, Paul T. Konkola, Michael H. Lim, Anthony J. Lochtefeld, Mitchell W. Meinhold, Rajesh Menon, Euclid E. Moon, Thomas E. Murphy, David G. Pflug, Kevin P. Pipe, Minghao Qi, Farhan Rana, Timothy A. Savas, Michael E. Walsh

Technical and Support Staff

James M. Daley, Cynthia A. Lewis, Edward R. Murphy

3.1 Nanostructures Laboratory

The Nanostructures Laboratory (NSL) at MIT develops techniques for fabricating surface structures with feature sizes in the range from nanometers to micrometers and uses these structures in a variety of research projects. The NSL includes facilities for lithography (photo, interferometric, electron-beam, and x-ray), etching (chemical, plasma and reactive-ion), liftoff, electroplating, sputter deposition, and e-beam evaporation. Much of the equipment, and nearly all of the methods, utilized in the NSL are developed in-house. Generally, commercial processing equipment, designed for the semiconductor industry, cannot achieve the resolution needed for nanofabrication, is inordinately expensive and lacks the required flexibility. The research projects within the NSL fall into three major categories: (1) development of submicron and nanometer fabrication technology; (2) short-channel semiconductor devices, optoelectronics, and microphotonics; and (3) periodic structures for x-ray optics, spectroscopy, atomic interferometry and nanometer metrology.

3.2 Scanning-Electron-Beam Lithography

Sponsors

Defense Advanced Research Projects Agency
Grant MDA972-97-1-000
University of California at Berkeley
Contract SA1645-25508PG
U.S. Air Force - Office of Scientific Research
Grant F49620-96-1-0126
U.S. Army Research Office
Grant DAAH04-95-1-0564
Grant DAAG55-98-1-0130

Project Staff

Mark K. Mondol, Professor Henry I. Smith

Figure 1 is a photograph of the scanning-electron-beam lithography system (VS-2A) located in the scanning-electron-beam lithography (SEBL) facility in Room 38-165. This instrument was obtained as a donation from IBM in November 1993. Its digital pat-

tern generator is based on a commercial high-performance array processor, which uses dual RISC processors. The system is capable of creating large-area patterns composed of multiple stitched fields. Conversion software has been developed which allows a CAD data file to be fractured and translated prior to exposure by the electron-beam tool.



Figure 1. Photograph of the VS-2A scanning-electron-beam lithography system. The operator is Research Specialist Mark Mondol.

The VS-2A can expose substrates up to 20 cm diameter at linewidths down to 70 nm. The goals of the SEBL facility are to: (1) provide the MIT research community with an in-house SEBL capability for writing directly on experimental device substrates; (2) advance state of the art in SEBL, particularly with regards to pattern placement accuracy and long-range spatial-phase coherence; and (3) pattern x-ray nanolithography masks for in-house use. To write concentric circular patterns, such as Fresnel zone plates, software was developed to generate arbitrary arcs of an annulus with user-specified start and finish radii and angles.

In 1998, the VS-2A was used to write: Fresnel zone plates, as phase masks, on quartz for experiments in zone-plate-array lithography; 100-nm features on quartz masks for UV contact lithography experiments; gratings for channel-dropping filters, with long range coherence, on x-ray masks; and alignment marks on x-ray masks for experiments on IBBI alignment. VS-2A was used in the direct-writing mode for projects on: magnetic storage; a super-luminescent LED using a two-dimensional photonic band gap; one-dimensional photonic bandgap structures; and three-dimensional photonic bandgap structures (Figure 2). VS-2A was also used extensively in experiments on spatial-phase-locked e-beam lithography.

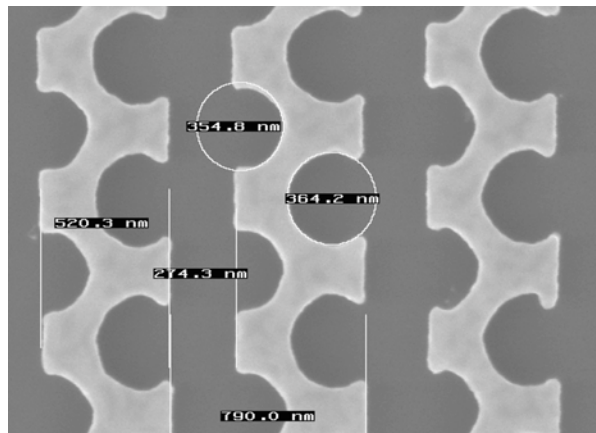


Figure 2. Scanning-electron micrograph of an early stage in the fabrication of a three-dimensional photonic bandgap (PBG) structure for the 1.5-micron wavelength, written with VS-2A. The micrograph shows the complex geometry and dimensional control necessary for this type of PBG structure. The design, which enables planar nano-fabrication technology to be used, was developed in Professor John D. Joannopoulos' group.

3.3 Spatial-Phase-Locked Electron-Beam Lithography

Sponsors

Defense Advanced Research Projects Agency
Grant MDA972-97-1-000
University of California at Berkeley
Contract SA1645-25508PG
U.S. Army Research Office
Grant DAAG55-98-1-0130

Project Staff

Nitza M. Basoco, Aleksandr Bernshteyn, Juan Ferrera, Dr. James G. Goodberlet, Mark K. Mondol, Professor Henry I. Smith

Spatial-phase-locked electron-beam lithography (SPLEBL) has been under development at MIT for several years and promises to reduce pattern-placement errors in electron-beam lithography systems to the nanometer level. Such high precision is essential for future integrated electronics and optics. Currently, SPLEBL is the only approach capable of achieving this goal. Nanometer precision in pattern placement is possible by incorporating feedback into the electron-beam lithography system. In SPLEBL, a low-level, periodic signal, derived from the interaction of the e-beam with a fiducial grid on the substrate, is used to continuously track the position of the e-beam while patterns are written. Any deviations of the

beam from an intended location are sensed, and corrections are fed back to the beam-control electronics to cancel errors in the beam's position.

Our goal this year has been to extend SPLEBL from an earlier one-dimensional demonstration to a two-dimensional demonstration. To accomplish this, several improvements in SPLEBL components have been required. Specifically, our tasks have been to (1) improve the fiducial grid which is patterned on the substrate and generates the periodic signal, (2) design and build a high-speed electron-beam dose modulator, and (3) develop a digital-signal processing algorithm which phase-locks to the periodic fiducial-grid signal and determines precisely the beam-position corrections.

The fiducial grid for SPLEBL typically provides a weak signal. To improve the signal quality and simplify patterning of the fiducial grid, we have developed a PMMA-based organic, scintillating polymer mixture. The composition, by weight, of the scintillator is PMMA (87%), naphthalene (8%), anthracene (2.5%) and 2,2'-p-phenylenebis-(5-phenyloxazole) (2.5%). PMMA is an electron-beam sensitive resist, and the other components provide the scintillation signal. Anthracene is an ultraviolet-sensitive scintillator; i.e., its scintillation is quenched after exposure to UV radiation, and, because of this property, a scintillating fiducial grid may be patterned easily in the polymer by exposing it to a UV standing wave. The measured quenching property of this resist-scintillator composition is shown in Figure 3.

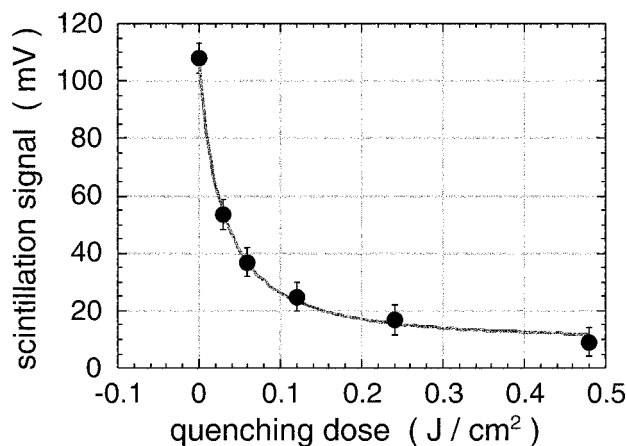


Figure 3. The quenching response of the scintillator-resist composition was measured after exposing it to 351 nm radiation. This radiation did not affect the electron-beam resist's properties.

A signal contrast of 2.8 was measured from a scintillating fiducial grating patterned in this polymer which is a substantial improvement upon the value of contrast (1.15) obtained in the previous demonstration of SPLEBL which employed backscattered electrons. We also observed that the UV irradiation did not affect the e-beam resist's properties. Hence, this polymer formulation incorporates both the e-beam resist and scintillating fiducial grid into a single layer, which is spun onto a substrate for patterning. We are also investigating bilayer schemes in which the resist and scintillating polymers may be spun onto the substrate separately.

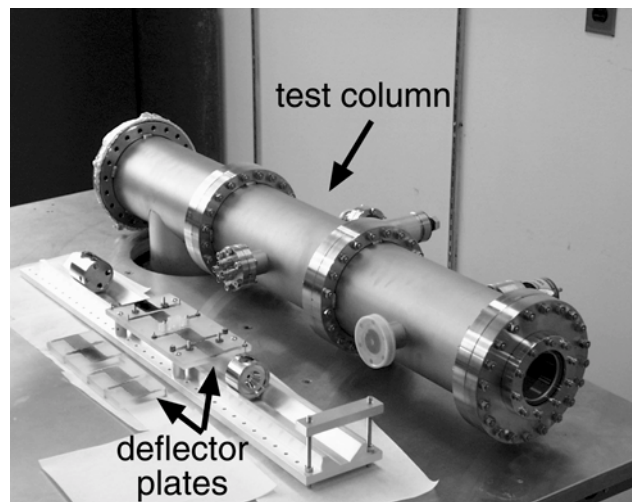


Figure 4. The quadra-deflection electron-beam dose modulator, shown in the foreground, consists of four electrostatic deflectors and an aperture plate. The quadra deflector will be tested in the bench-top electron-beam column shown in the background.

In SPLEBL, a high-speed electron-beam dose modulator must be used to switch the e-beam rapidly from a "fully-on" state, when exposing patterns, to a "partly-on" state, when moving between patterns. The "partly-on" state permits continuous monitoring of the e-beam's position, i.e., constant feedback. The dose modulator must be capable of switching in short times, ~ 1 ns, to permit patterning at high data rates. We have designed an electrostatic deflection apparatus (quadra deflector) which enables high-speed dose modulation. The quadra deflector consists of four pairs of deflection plates which locally deviate the electron-beam path between two current-limiting apertures. The quadra deflector is shown in Figure 4, along with a bench-top electron-beam column which is being assembled to test the deflector. In a simple electrical measurement the quadra deflector's plates were switched in 6.0 ns, as shown in the graph of

Figure 5. This time was primarily determined by the slow current driver used to switch the plates and cabling between the driver and plates. The response of the plates is calculated to be about 0.75 ns.

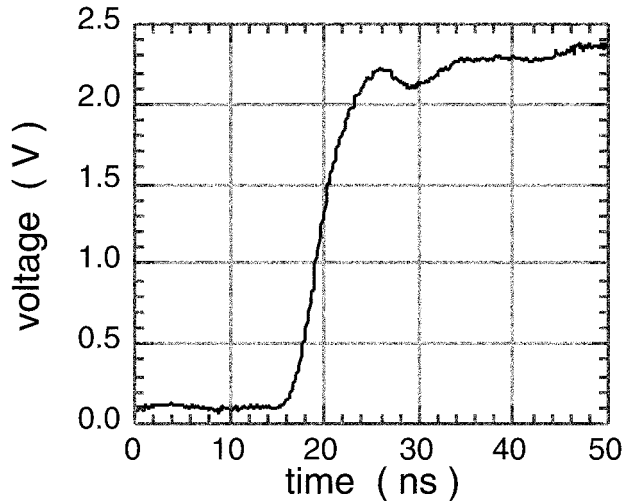


Figure 5. The electrical switching time of the quadra deflector's plates were measured to be about 6.0 ns. This risetime was primarily determined by the current driver, about 4.7 ns, and cabling used to connect the plates and driver. The calculated switching time for the plates is about 0.75 ns.

We are investigating the application of digital-signal processing to the SPLEBL architecture. In the previous proof-of-concept experiment, analog circuitry was used to demonstrate SPLEBL in one dimension. We believe digital signal processing (DSP) techniques are better suited for the 2-D SPLEBL system because of greater flexibility in feedback algorithms and greatly reduced complexity in circuit design. To develop a robust and efficient DSP algorithm for SPLEBL, we must first develop a realistic model of the electron-beam system and expected fiducial grid signal. This simulated signal, which reflects properties of the organic scintillator and system noise, will be used to test the DSP phase-locking algorithms.

We have begun programming the signal simulator which incorporates such factors as scintillator quenching response, contrast of the UV standing wave used to pattern the fiducial grating, and convolution of the electron-beam profile and fiducial-grid pattern. Two results from the simulator are shown in Figure 6. The graphs show the expected scintillation contrast from two types of organic scintillating fiducial grids. In one case, lower trace, the scintillating polymer has the nonlinear quenching response shown in

Figure 1. For the other case, the quenching response is modeled as linear. Clearly, the linear case is more desirable, and we will investigate ways to improve the quenching response of the scintillator. The signal simulator will be complete when we have added noise, characteristic of the e-beam system, to the signal.

After completing experiments with the dose modulator and testing phase-locking algorithms, we will be ready to demonstrate two-dimensional SPLEBL. We anticipate a demonstration in the coming year.

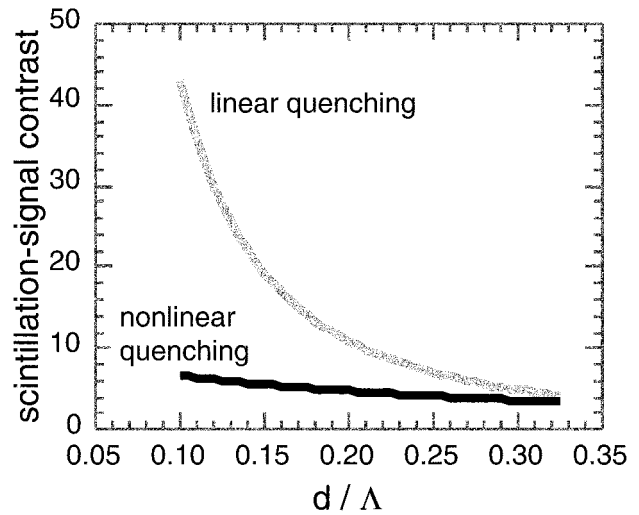


Figure 6. The contrast expected from a scintillating fiducial grid with a linear quenching response is better than that from our existing polymer formulation. The graph was generated using a signal simulator that is being developed to test DSP phase-locking algorithms for SPLEBL.

3.4 X-Ray Nanolithography

Sponsors

Defense Advanced Research Projects Agency/
U.S. Navy - Naval Air Systems Command
Contract N00019-98-K-0110

Project Staff

Dr. David J.D. Carter, James M. Daley, Michael H. Lim, Euclid E. Moon, Professor Henry I. Smith

For several years, we have been developing the tools and methods of x-ray nanolithography. We have explored the theoretical and practical limitations and endeavored to make its various components (e.g., mask-making, resists, electroplating, sources, align-

ment, etc.) reliable and “user-friendly.” Because of the critical importance of x-ray mask technology, we discuss this in a separate section.

Our sources for x-ray nanolithography are simple, low-cost electron-bombardment targets, typically Cu_L ($\lambda = 1.32 \text{ nm}$), separated by a $1.4 \text{ }\mu\text{m}$ -thick SiN_x vacuum window from a helium-filled exposure chamber. In the future, we hope to replace the Cu_L sources with a higher-flux plasma-focus source.

In earlier research, we showed that for wavelengths longer than 0.8 nm , the important limit on resolution is diffraction in the gap between mask and substrate. With a Cu_L source, a 50 nm feature must be exposed at a mask-to-substrate gap of less than about three microns in order to maintain good process latitude. A 25 nm feature would require a gap of less than a micron. For very small features, we eliminate the gap and use contact between the substrate and the flexible membrane mask, induced by electrostatic forces or partial vacuum and atmospheric pressure. This technique has allowed us to replicate features as small as 25 nm in size in a practical reproducible way. Figure 7 shows scanning electron micrographs of device pattern replication by liftoff onto a substrate with feature sizes less than 40 nm . The x-ray mask is shown on top and the lifted-off pattern is on the bottom.

To create the x-ray masks, the pattern is first written by electron-beam lithography onto an x-ray “mother” mask, using either our in-house e-beam system or in a collaboration with the Naval Research Laboratory in Washington, D.C. The e-beam written pattern is developed, and gold is electroplated into the resist mold. A negative replica, or “daughter” mask is created by exposing with the mother mask using soft-contact x-ray nanolithography. Finally, the daughter mask is exposed onto the device substrate.

Recent work has focused on investigating process latitude at these extremely fine feature sizes. Figure 8 shows how developed linewidth changes for up to

50% overdevelopment (i.e., developing for 50% longer than it takes for the feature to clear) as a function of linewidth. As can be seen from the plot, the measured feature on the substrate remains within a $\pm 10\%$ process window (within the accuracy of the measurement) for isolated features as small as 30 nm and for dense features (greater than 1:3 line:space ratio) as small as 45 nm . This data indicates that soft-contact x-ray lithography is extremely robust and offers very wide process latitude.

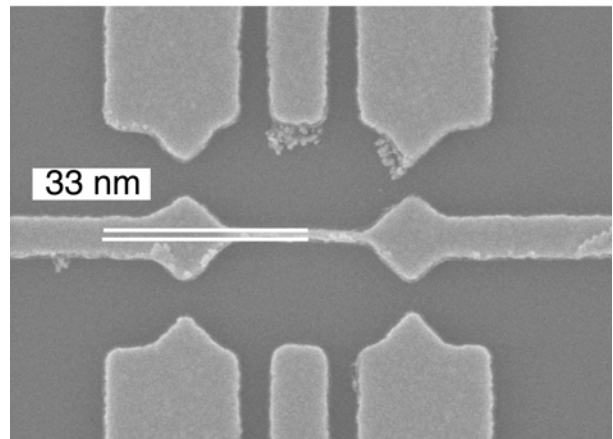
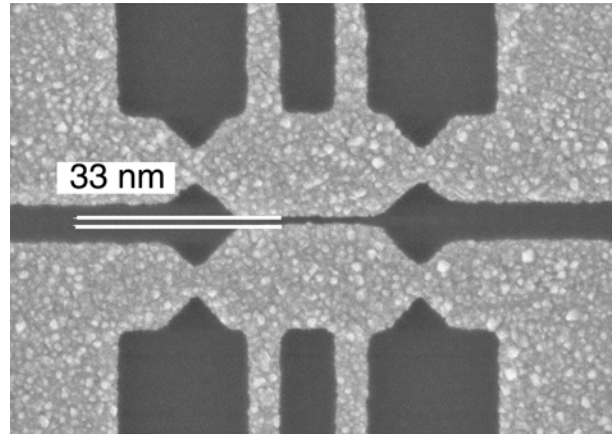


Figure 7. Scanning electron micrographs of device pattern replication by liftoff onto a substrate with feature sizes less than 40 nm . The x-ray mask is shown on top and the lifted-off pattern is on the bottom.

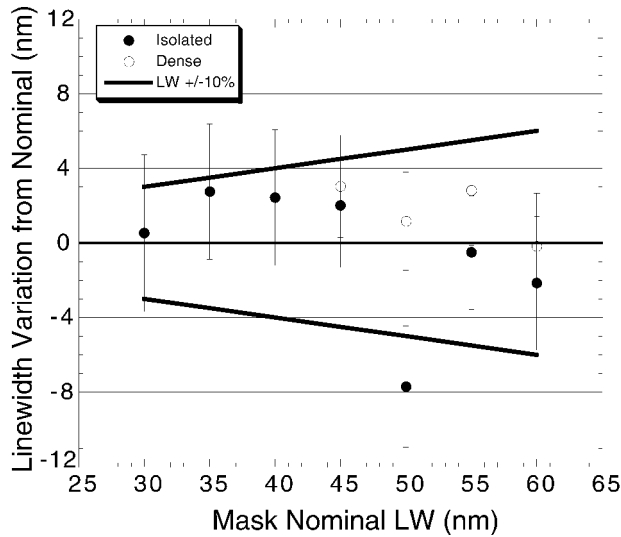


Figure 8. Plot of linewidth variation from nominal (i.e., developed for the time required to clear features) for up to 50% overdevelopment. Isolated features stay within a $\pm 10\%$ process window for features as small as 30 nm. Dense (line:space ratio of 1:3 or greater) features remain in the process window for features as small as 45 nm.

3.5 Zone-Plate-Based X-Ray and UV Projection Lithography

Sponsors

Defense Advanced Research Projects Agency
 Grant MDA972-97-1-000
 University of California at Berkeley
 Contract SA1645-25508PG

Project Staff

Dr. David J.D. Carter, Darío Gil, Rajesh Menon, Professor Henry I. Smith

Soft-contact x-ray nanolithography is unique to MIT, and, although suitable for research, it is considered incompatible with manufacturing. Accordingly, we are developing an alternative approach that would preserve the desirable features of x-ray lithography while circumventing the need to bring the mask into intimate contact with the substrate. Our proposed solution, zone-plate array lithography (ZPAL), is a maskless projection lithography system that employs an array of Fresnel zone plates. As illustrated in Figure 9, an array of Fresnel zone plates focuses an incident beam of 4.5 nm x-rays, forming an array of diffraction-limited spots on a substrate. Writing is done via a dot-matrix-printing strategy, with the individual beams multiplexed by an array of micromechanical shutters located upstream of the zone-plate

array. The resolution or spot size is approximately equal to the width of the outermost zone. Hence, the resolution of the system is determined by one's ability to make the zone plates by e-beam lithography and dry etching.

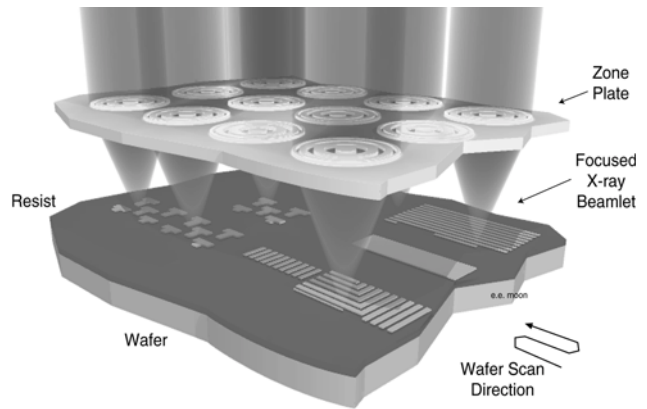


Figure 9. Schematic of a maskless projection lithography scheme that employs 4.5 nm x-rays focused to an array of diffraction-limited spots. Writing is done via a dot-matrix scheme, with micromechanical shutters modulating the x-ray flux to each zone plate. With 4.5 nm x-rays, 25-nm or smaller spot sizes should be attainable.

The maskless projection system, shown in Figure 9, would eliminate the need for a mask, potentially decreasing the overall cost of ultrafine lithography. Moreover, for patterning at the limits of the lithographic process, the 4.5 nm photon offers the optimal combination of minimal proximity effects, short enough wavelength to enable large depth-of-focus, and sufficient penetration to eliminate the need for surface-interaction resists. Although the best available source of 4.5 nm photons with the necessary temporal and spatial coherence is an undulator attached to a synchrotron, we are using a C_K ($\lambda = 4.5$ nm) electron bombardment source for purposes of research. With this source, we intend to prove the resolution limits of ZPAL.

At the same time, to explore system design issues, an experimental UV ZPAL system has been constructed. We have fabricated phase-shifting zone plates in quartz and built an apparatus that ensures the substrate is in the correct focal plane of the zone plate array. With this setup, the results shown in Figure 10 were obtained. Since then, we have added multiplexing capabilities to the system by means of an array of commercially available Texas Instruments micromechanical reflecting mirrors with promising preliminary results. With the acquisition of a sub-4 nm precision stage, we should be able to expose arbitrary patterns that extend among many zone

plate unit cells. This UV system, in addition to providing maskless lithography capabilities, should be a good proving ground for multiplexing and stage coordination issues for x-ray ZPAL.

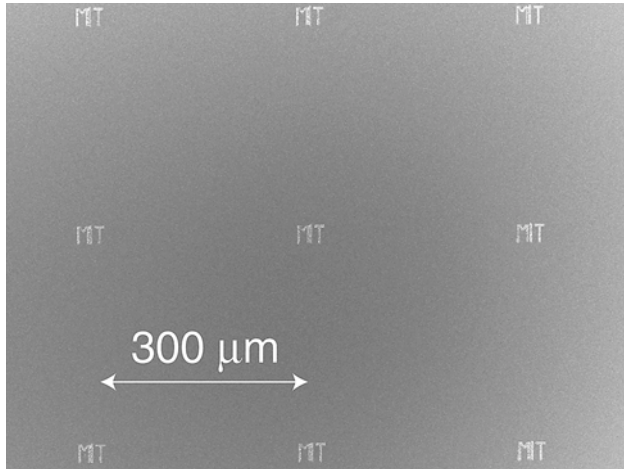


Figure 10. Scanning electron micrograph of a pattern in PMMA after development. The 3 x 3 array of patterns were written in parallel with a zone-plate array focusing the deep-UV radiation from an ArF laser ($\lambda = 193$ nm). For this example, the stage was moved by hand and no multiplexing was performed.

3.6 Improved Mask Technology for X-Ray Lithography

Sponsors

Defense Advanced Research Projects Agency/
U.S. Navy - Naval Air Systems Command
Contract N00019-98-K-0110

Project Staff

James M. Daley, Juan Ferrera, Michael H. Lim, Ken-ichi Murooka, Edward R. Murphy, Kevin P. Pipe, Professor Henry I. Smith

At feature sizes of 100 nm and below the mask-to-substrate gap, G , must be less than ~ 10 μm . Thus, for nanolithography the mask membrane should be considerably flatter than 1 μm , preferably ~ 100 nm. Our mask technology is based on low-stress, Si-rich silicon nitride, SiN_x . This material is produced in a vertical LPCVD reactor. Membranes of SiN_x can be

cleaned and processed in conventional ways. For absorber patterns, we electroplate gold onto the membrane, using a specially designed apparatus, after resist exposure and development. A Ti/Au plating base is deposited on the membrane prior to resist coating. To pattern periodic structures on the x-ray masks, we use interferometric lithography (IL); and for patterns of arbitrary geometry, we use e-beam lithography—either at the MIT SEBL facility or in collaboration with Naval Research Laboratory (NRL). We use our Leo SEM and Digital Instruments STM/AFM to inspect our x-ray masks for defects. Radiation hardness for SiN_x membranes remains a problem at dose levels corresponding to production (i.e., millions of exposures). For research purposes, however, the material is entirely acceptable.

Currently, we are developing a pellicled x-ray mask, depicted in Figure 11. This mask has several advantages over the traditional x-ray mask: (1) the critical absorber pattern can be protected within a dust-free enclosure; (2) the membrane can be cleaned using aggressive techniques without damaging the absorber pattern; (3) any dust that falls onto the pellicle will not be imaged onto the substrate due to diffraction and penumbral blurring; (4) the resulting membranes are flat to less than 30 nm, as shown in Figure 12; and (5) one can place a fiducial grid on the frontside of the membrane to track distortions that might occur during the processing and lifetime of the mask. To fully take advantage of this x-ray mask configuration, we must be able to anodically bond the membrane to the mask frame with minimal distortion.

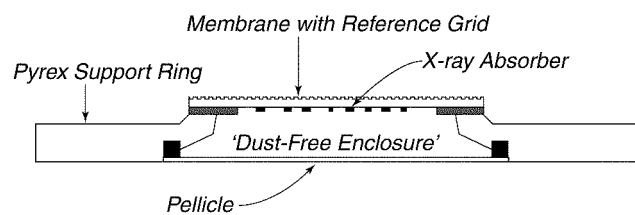


Figure 11. Schematic showing how the absorber pattern on an x-ray mask can be protected from the accumulation of dust and other contamination by enclosing it between the membrane and a pellicle. Dust accumulated on the membrane can be removed by aggressive techniques. The grid is to enable measurement of in-plane distortion via the HPSI interferometer (Figure 13).

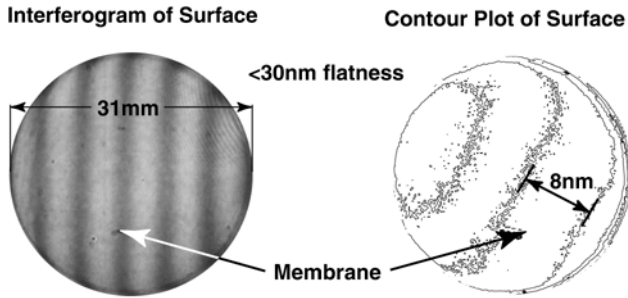


Figure 12. Interferogram of the top surface of an x-ray mask membrane bonded to a Pyrex support ring as in Figure 11, indicating a flatness better than ~30 nm over most of the membrane area.

To analyze the distortions that occur during the anodic bonding of the membrane to the pyrex ring, we have developed a broadly applicable, nondestructive, global, membrane-distortion measurement technique. This technique uses a holographic phase-shifting interferometer (HPSI) based on the apparatus that Ferrera, et. al.¹ used to measure the phase distortion of interferometrically-generated gratings.

The HPSI system is based on the interferometric lithography (IL) system we use to generate large-area, highly-coherent gratings. Figure 13 is a schematic of the IL apparatus, configured as a HPSI system. The IL system splits a laser beam ($\lambda = 351 \text{ nm}$) and forms two mutually coherent spherical waves, which interfere at the substrate at a half-angle θ . The standing wave created at the substrate surface is used to expose photoresist. After development, the grating is present on the substrate surface or can be etched into it. The IL system is configured as a holographic interferometer simply by mounting the IL-generated grating on the substrate platform and placing a fluorescent screen in front of one of the spatial filters, as depicted in Figure 13. A fringe pattern appears on the screen, which is due to the superposition of two wave fronts: one reflected from the substrate surface and the other back-diffracted from the grating. If the grating has suffered no distortion between exposure and reinsertion, the reflected and back-diffracted beams will be identical and no fringes will be observed on the screen. Any in-plane distortion of the grating will result in a fringe pattern.

A CCD camera is used to capture the fringes. To increase the precision, a phase-shifting measurement is implemented, by changing the phase of one of the arms and acquiring several images. In order to use this apparatus to measure the in-plane distortion, we etch shallow IL-generated gratings into the membrane.

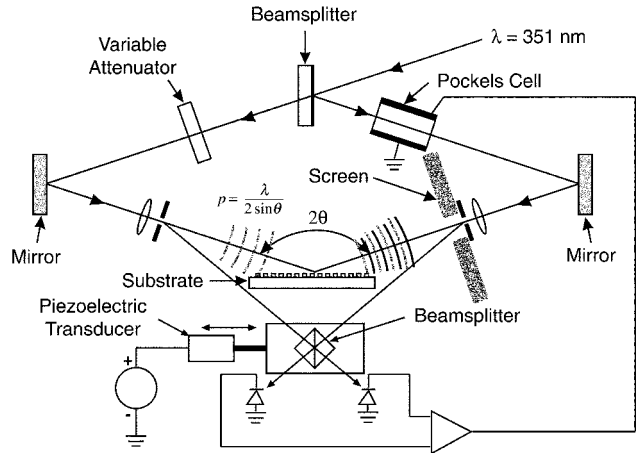


Figure 13. A schematic of the holographic phase-shifting interferometer (HPSI) based on the interferometric lithography system that we use to generate highly-coherent gratings.

We first form a membrane that is 54 mm in diameter and 1 μm thickness. Next we pattern 400 nm period gratings into a number of membranes, including one that we set aside as a reference. Then we anodically bond these membranes to pyrex frames, except for the reference membrane. Afterwards, we place the reference membrane into the HPSI system and align the system so that it exactly matches the conditions that previously exposed the grating; good alignment is ensured by minimizing the number of fringes in the interference pattern. Finally, we place the flip-bonded x-ray mask into the HPSI system and acquire an interferogram; we then analyze the interferogram using the 5-step Hariharan algorithm. The process flow for the measurement is shown in Figure 14. A typical interferogram is shown in Figure 15a.

¹ J. Ferrera, M.L. Schattenburg, and H.I. Smith, "Analysis of Distortion in Interferometric Lithography," *J. Vac. Sci. Technol. B*, 14: 4009–13 (1996).

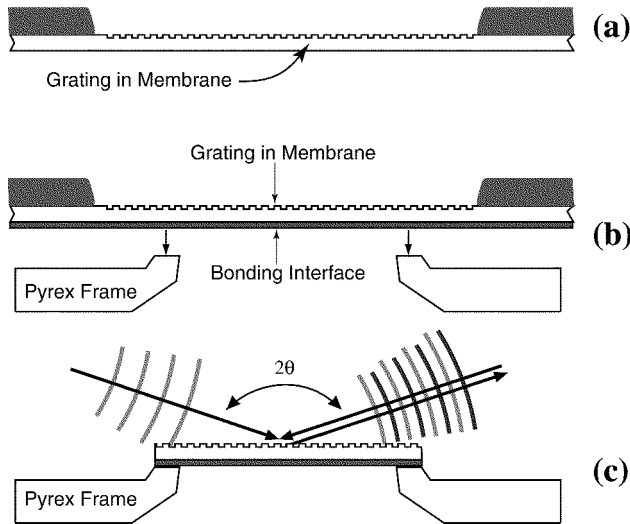


Figure 14. The process used for measuring the distortion that occurs during anodic bonding: (a) a 400 nm period grating is etched into the membrane; (b) the membrane is bonded to a pyrex frame; (c) the completed mask is placed in the HPSI for analysis.

Analysis of this data indicates that the period of the grating contracted from 400 nm to 399.97 nm. Figure 15b shows a one-dimensional distortion plot extracted from the interferogram. As a check, we measured the period contraction using a different method. The half-angle of recombination of both beams can be changed by translating the substrate in the direction perpendicular to its surface; a positive translation shortens the period of the standing wave. We employed this effect to directly measure the period change of the grating by translating the substrate stage forward until the fringes were minimized. After moving the stage forward by $130 \mu\text{m}$, the fringes were minimized, indicating that the period of the distorted grating was 399.97 nm which agrees with the value extracted from the interferogram analysis. We are currently working to extend the mea-

surement system to two dimensions as well as attempting to minimize the distortion caused by anodic bonding.

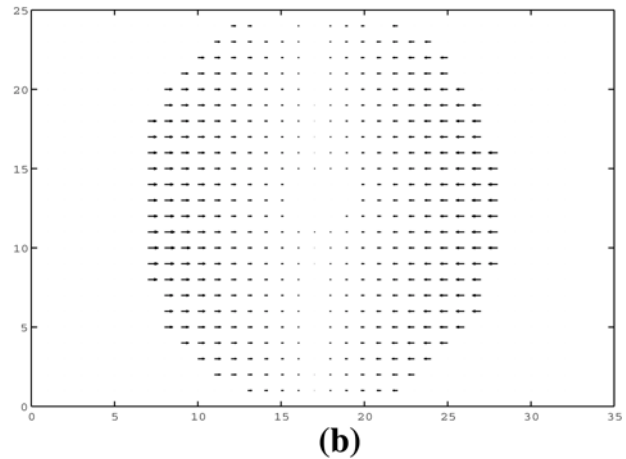
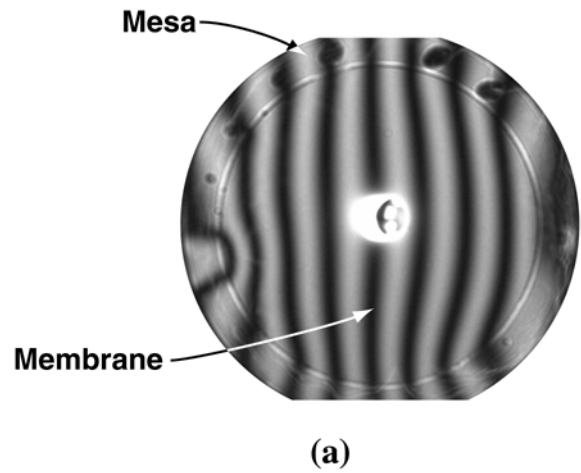


Figure 15. Measurement and analysis results from the HPSI; (a) the interferogram that results when the completed mask is placed back into the HPSI; (b) the distortion map calculated from (a) showing the grating contraction and the resulting in-plane distortion due to the anodic bonding.

3.7 Nanometer-level Feedback-Stabilized Alignment and X-ray Exposure System

Sponsors

Defense Advanced Research Projects Agency
 Grant MDA972-97-1-000/
 Suss Advanced Lithography
 Contract PO S1668
 University of California at Berkeley
 Contract SA1645-25508PG

Project Staff

Dr. Patrick N. Everett, Euclid E. Moon, Professor
 Henry I. Smith

An experimental high-precision, x-ray exposure and alignment system has been constructed that employs interferometric broad-band imaging (IBBI) for alignment. (Figure 16a). The objective of this system is to achieve ~1 nm overlay. The IBBI scheme employs grating and checkerboard type alignment marks on mask and substrate, respectively, which are viewed through the mask from outside the x-ray beam at a Littrow angle of 15 degrees with f/10 optics and a 110 mm working distance. Each mark consists of two gratings (or checkerboards) of slightly different periods, p_1 and p_2 , arranged so that p_1 is superimposed over p_2 , and p_2 over p_1 during alignment. Alignment is measured from two identical sets of moiré fringes, projected onto a CCD, that move in opposite directions as the mask is moved relative to the substrate. The relative spatial phase of the two fringe sets signifies alignment.

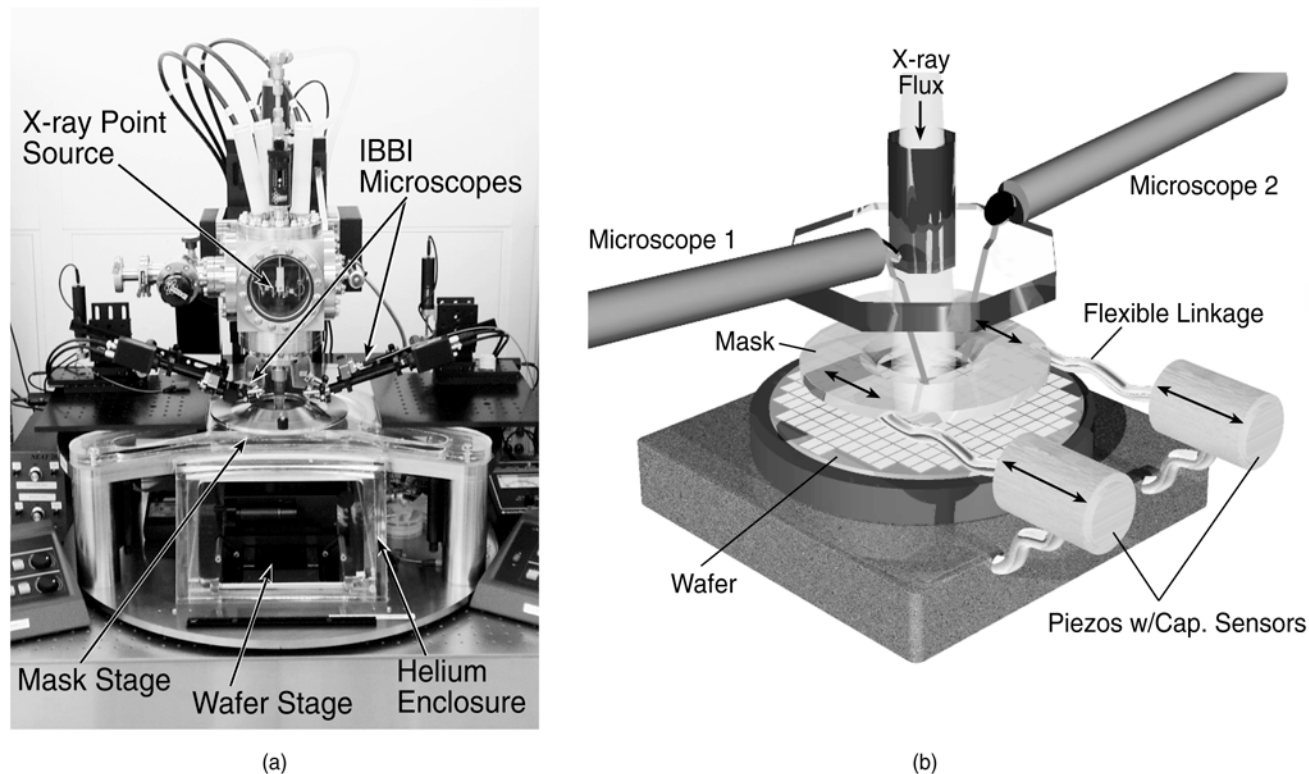


Figure 16. (a) X-ray exposure and alignment system. Mask and wafer are located in a helium ambient and exposed to x-rays. IBBI microscopes observe alignment through a viewport before and during exposure. (b) Schematic of displacement experiments monitored by IBBI. Alignment is observed at two marks simultaneously by two microscopes. The relative mask-wafer position is controlled by piezos with integral capacitive sensors.

Experiments depicted schematically in Figure 16b demonstrate that the displacement scale observed by IBBI is consistent with the scale of a calibrated capacitive sensor associated with a closed-loop piezoelectric drive. Figure 17 shows alignment data

read simultaneously from two microscopes, during times when the piezos were alternately scanning and stationary. The difference between the average IBBI reading and the piezo displacement was found to be within 1.5%.

Experiments showed that IBBI is self-consistent when viewed by two independent optical systems. Two microscopes observed the same mark, as shown in Figure 18, while taking readings alternately. The independent readings had a mean difference of 0.01 nm and a standard deviation of 0.66 nm.

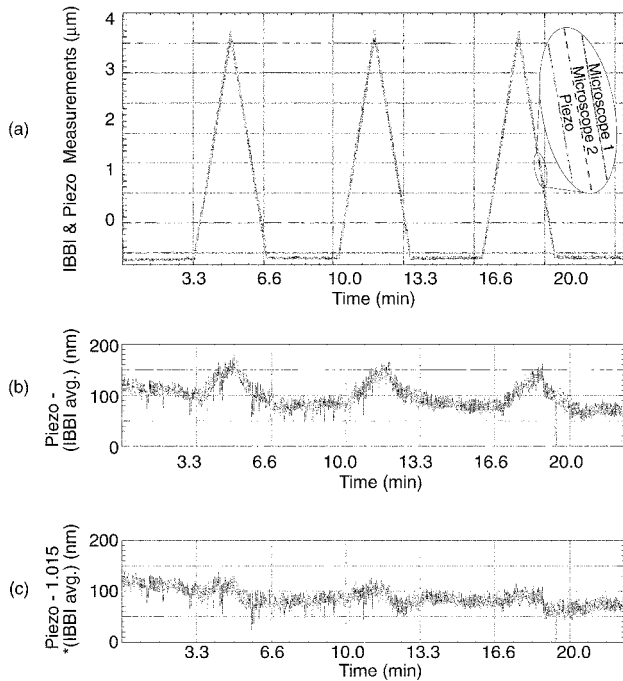


Figure 17. Agreement between two simultaneous IBBI measurements and piezo/capacitor drives during 3.7 μm back-and-forth scan of mask. (a) IBBI measurements and piezo displacements throughout three scan/rest cycles. (b) Difference of piezo and average IBBI displacement readings, showing residual scale error. (c) Best-fit found with scale increase of 1.5%. The residual scale error is attributed to flexing of the 10 cm of metal separating mask and piezos, and possible pattern magnification during E-beam mask writing.

The ability of IBBI to observe nanometer-level alignment during x-ray exposures implies that disturbances can be corrected during the course of an exposure. Figure 19a shows drift and vibration of the exposure/alignment system over a period of several hours, with the system running open loop. Feeding back a correction signal to the piezos (Figure 19b) results in alignment that is stabilized to a mean of 0.0 nm and a standard deviation of 1.4 nm.

The unique capabilities of IBBI alignment are being employed in the fabrication of a variety of electronic and optical devices, including 25 nm effective-channel-length n-MOS transistors.

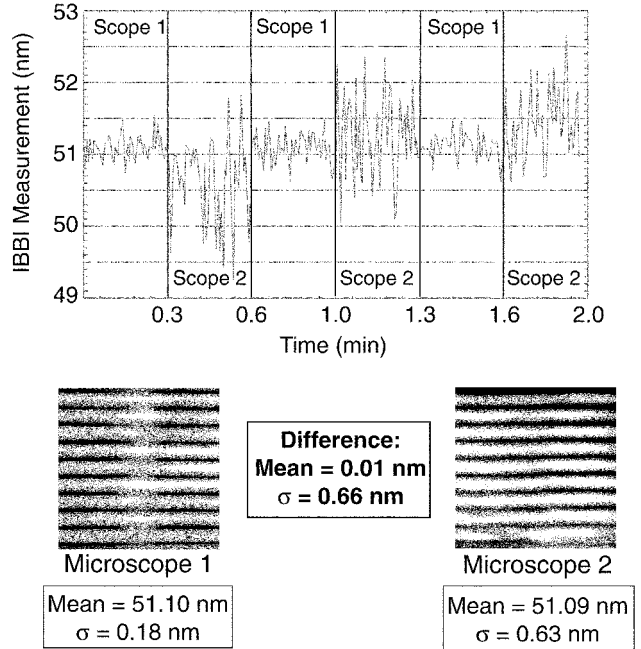


Figure 18. Two IBBI microscopes alternately observe the same alignment mark from opposite directions, with the mask locked to the wafer at a 3 μm gap. Measurements agree to within $\sigma = 0.66$ nm.

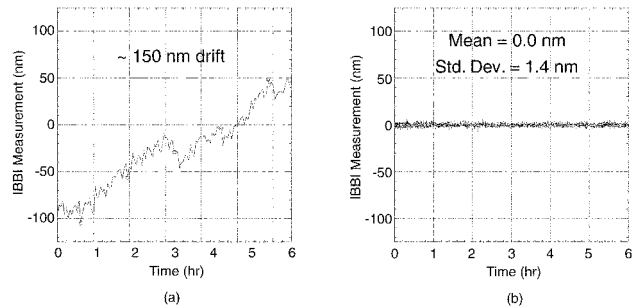


Figure 19. Six-hour alignment data. (a) Open-loop operation. (b) Closed-loop operation.

3.8 Interferometric Lithography

Sponsors

U.S. Air Force - Office of Scientific Research
Grant F49620-96-1-0126

U.S. Army Research Office
Grant DAAG55-98-1-0130

U.S. Navy - Office of Naval Research
Grant N00014-96-1-0802

Project Staff

James M. Carter, Maya S. Farhoud, Juan Ferrera, Robert C. Fleming, Timothy A. Savas, Michael E. Walsh, Dr. Mark L. Schattenburg, Professor Henry I. Smith

Interferometric lithography is preferred for the fabrication of periodic and quasi-periodic patterns that must be spatially coherent over large areas. For spatial periods down to 200 nm, an argon ion laser is used in a Mach-Zehnder configuration, with a fringe-locking feedback system, as illustrated in Figure 20. This scheme produces large area (10 cm-diameter) gratings with long-range, spatial-phase coherence. Fringe locking ensures reproducibility of exposure.

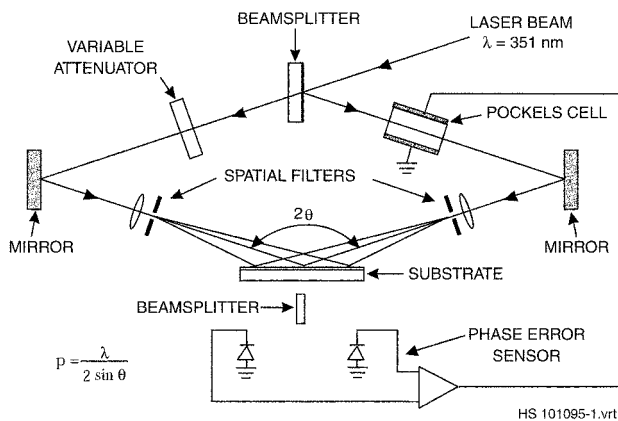


Figure 20. Schematic of the MIT interferometric lithography system. The system occupies a 2×3 m optical bench in a class 100 clean environment. The beamsplitter directs portions of the two interfering spherical beams to photodiodes. A feedback locking is achieved by differentially amplifying the photodiode signals and applying a correction to the Pockels cell which phase shifts one of the beams.

The gratings and grids produced are used as fiducials in spatial-phase-locked electron-beam lithography and in a new approach to metrology for the sub-100 nm domain. In addition, a wide variety of applications, from ultra-high-density magnetic information storage to atom-beam interferometry, depend on interferometrically produced gratings and grids. These applications are separately described in this report.

For spatial periods below 200 nm, a source wavelength below 200 nm must be used. Since such sources have limited temporal coherence, one is forced to employ an achromatic scheme, as shown in Figure 21. The source is an ArF laser (192 nm wave-

length). A collimating lens, polarizer, and scanning system are interposed between the source and the interferometer in order to achieve reasonable depth-of-focus and large exposure areas. We also use a white light interference principle to insure equal path lengths in the two interferometer arms. Using this system, gratings and grids of 100 nm period (nominally 50 nm lines or posts) are obtained in PMMA on top of an antireflection coating. Figure 22 shows a 100 nm-period grid etched into Si following achromatic interferometric lithography. Grids of Si posts are being used to investigate photo- and electro-luminescence which may result from charge-carrier quantum confinement.

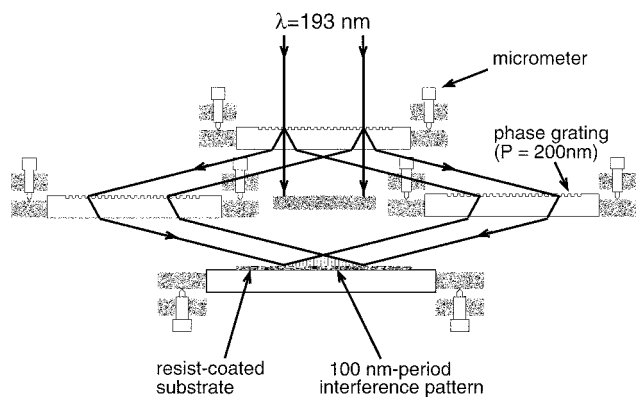
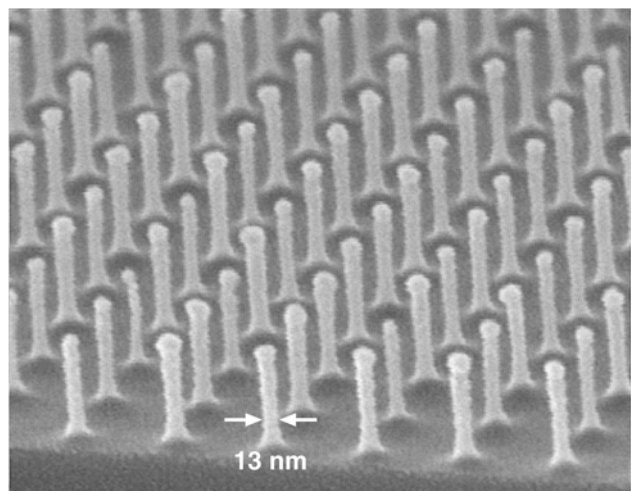


Figure 21. Achromatic interferometric lithography (AIL) configuration employed to produce 100 nm-period gratings and grids.



100nm-period posts in Si

Figure 22. Scanning electron micrograph of a 100 nm-period grid, exposed in PMMA on top of an antireflection coating, and transferred into Si by reactive ion etching.

To obtain spatial periods below 100 nm, a source wavelength below 100 nm and an achromatic scheme must be employed. We have established a collaboration with the University of Wisconsin, in which we will utilize an undulator light source (13 nm wavelength) incorporated into their synchrotron. An achromatic interferometer, currently being designed and built, will be capable of exposing 50 nm-period gratings and grids in resist.

3.9 A Two-Dimensional Photonic-Band-Gap Super-Luminescent Light-Emitting Diode

Sponsors

National Science Foundation

Grant DMR 94-00334

U.S. Army Research Office

Grant DAAG55-98-1-0474

Grant DAAG55-98-1-0080

Project Staff

Alexei A. Erchak, Steven G. Johnson, K.-Y. Lim, Mark K. Mondol, Daniel J. Ripin, Dr. Shanhui Fan, Professor Erich P. Ippen, Professor John D. Joannopoulos, Professor Leslie A. Kolodziejski, Dr. Gale S. Petrich, Professor Henry I. Smith

A photonic band gap (PBG) is the optical analog of an electronic band gap in a semiconductor. A periodic variation in the dielectric constant forbids certain photon energies within the semiconductor. Specifically, a two-dimensional PBG inhibits the propagation of light within a certain range of frequencies in any direction in a plane. In this work, a two-dimensional PBG is fabricated in the top cladding layer of an InGaP/InGaAs quantum well structure emitting at $\lambda = 980$ nm. The photonic crystal is designed so that the emission wavelength lies inside the photonic band gap and hence does not couple to guided modes within the semiconductor. Coupling to the guided modes is a major source of loss in conventional light-emitting diodes. In the structure being fabricated, this problem is greatly reduced, and the amount of light radiated from the device is enhanced.

The 2-D PBG LED consists of an InGaP/InGaAs active region, an Al_xO_y spacer layer and an $\text{Al}_x\text{O}_y/\text{GaAs}$ distributed bragg reflector (DBR). Figure 23 shows a schematic of the structure along with a completed structure. The 2-D photonic crystal is created

by a hexagonal lattice of holes within the upper InGaP cladding layer with a hole-to-hole spacing of 315 nm and a hole diameter of 220 nm. These dimensions center the photonic band gap around the 980 nm emission wavelength of an InGaP/InGaAs quantum well structure. The holes do not penetrate the InGaAs quantum well region, however, to minimize surface carrier recombination. Moreover, the active quantum well region lies on top of a DBR designed to reflect the 980 nm light. The DBR consists of alternating layers of GaAs and Al_xO_y to achieve high dielectric contrast between the layers which leads to a DBR with a wide stop band. The active region is separated from the DBR by an Al_xO_y buffer layer. Separation by a low index layer forces a larger portion of the emitted light to have normal incidence on the DBR, which increases the amount of reflected light.

The fabrication of the 2-D PBG LEDs utilizes gas-source molecular beam epitaxy, direct-write electron-beam lithography, reactive-ion etching (RIE) and oxidation processes. The device structure is grown using gas-source molecular beam epitaxy. The separation layer is initially grown as $\text{Al}_{.98}\text{Ga}_{.02}\text{As}$ and the DBR consists of AlAs and GaAs layers. A SiO_2 layer is deposited on the grown structure using plasma enhanced chemical vapor deposition. The holes are defined in PMMA by direct-write electron-beam lithography. The electron beam writes a square pattern in the PMMA to represent each hole. The beam size, however, is larger than the step size for translating the electron beam. This leads to the desired circular pattern following development.

The PMMA is used as a mask in transferring the hexagonal pattern to the SiO_2 layer using RIE. This is accomplished by RIE with a CHF_3 plasma using 15 second steps in between 1 minute cool-down steps, during which the electrode is back-cooled with He gas flow. The purpose of the cool-down step is to prevent flowing of the PMMA mask. The SiO_2 mask is subsequently used in the RIE of the holes into the upper InGaP cladding layer using RIE with a CH_4/H_2 plasma in a 1:4 gas flow ratio. The mesas are next defined using photolithography followed by RIE. The final step in the device fabrication is the wet thermal oxidation of the $\text{Al}_{.98}\text{Ga}_{.02}\text{As}$ separation layer and the AlAs DBR layers. Figure 24 is a scanning electron micrograph of the hexagonal array of holes within the upper InGaP cladding layer.

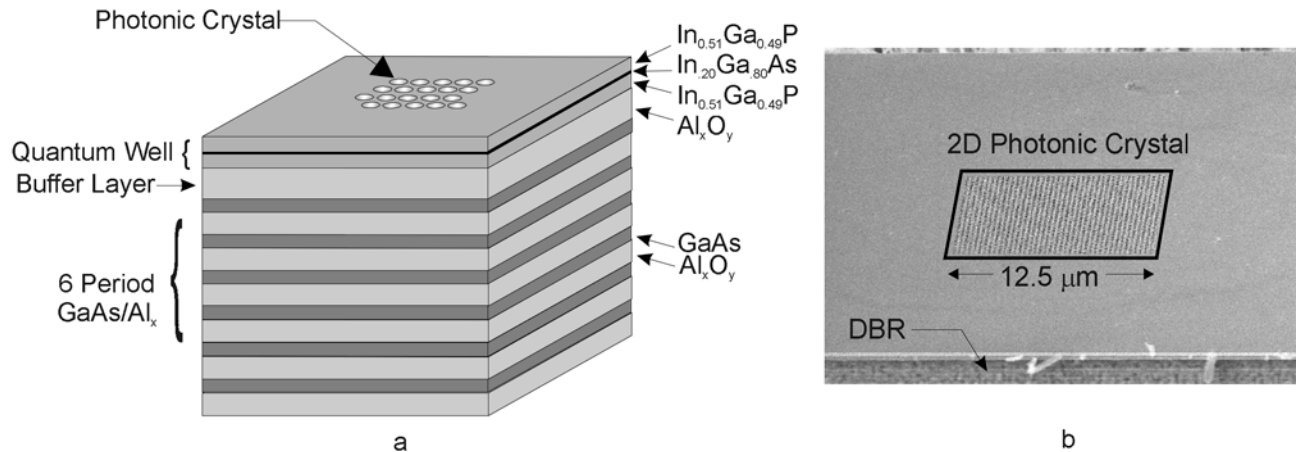


Figure 23. (a) 2-D PBG light emitting diode structure. The InGaP/InGaAs quantum well structure emits at $\lambda = 980$ nm. The active region is separated from the DBR by a low refractive index Al_xO_y separation layer. This separation increases the amount of emitted light reflected from the DBR. A hexagonal lattice of holes in the top layer of the device eliminates coupling of emitted light to guided modes. (b) SEM micrograph of 2-D PBG light emitting diode.

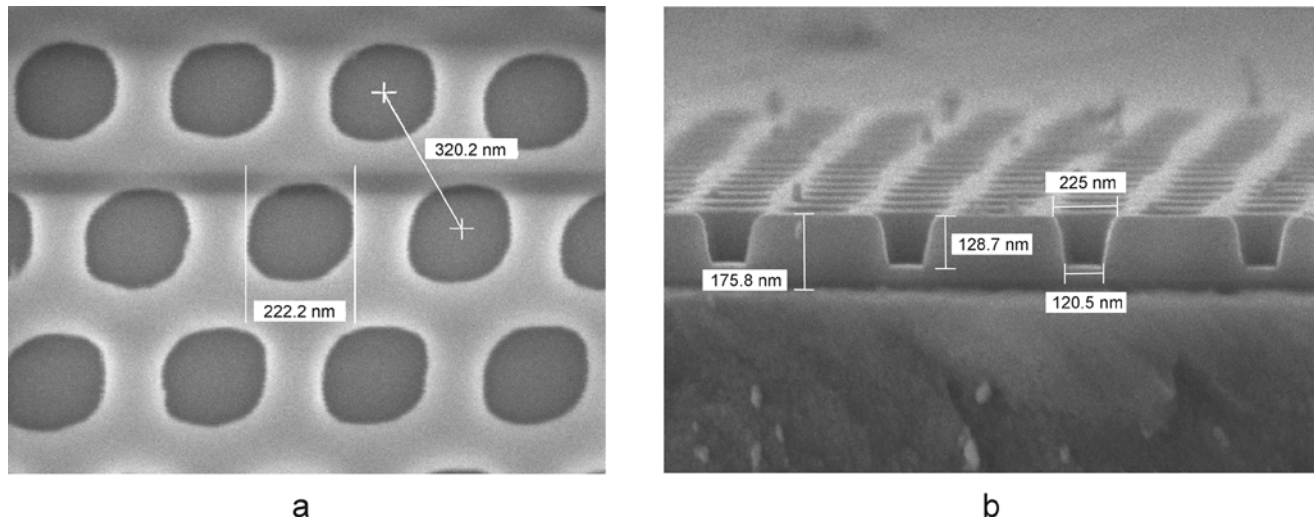


Figure 24. (a) Hexagonal array of holes forms a photonic crystal in the top InGaP layer of the LED. The holes are designed to forbid the guiding of $\lambda = 980$ nm light and hence increase the amount of light radiating from the device. (b) Cross-sectional view of 2-D PBG. The holes do not penetrate the InGaAs quantum well to avoid surface recombination.

Currently, the devices are being tested using cathodoluminescence. A high energy beam of electrons excites carriers within the active region which subsequently recombine in the quantum well. The intensity of the $\lambda = 980$ nm light emitted from the quantum well is measured using a Ge detector.

The intensity of light extracted from a device containing the 2-D PBG is compared to that of a device without the PBG. Simulations have shown that this structure should demonstrate at least a five-fold increase in extraction efficiency as compared to the same device without the presence of the photonic crystal.

3.10 Fabrication of Large Area Nanomagnet Arrays for Ultrahigh Density Magnetic Data Storage

Sponsors

Defense Advanced Research Projects Agency/
University of New Orleans
Grant 357-30-5114
National Science Foundation
Grant DMR 98-71539

Project Staff

Mathew C. Abraham, James M. Carter, Maya S. Farhoud, Yaowu Hao, Min-ha Hwang, Timothy A. Savas, Michael E. Walsh, Professor Caroline A. Ross, Professor Rajeev J. Ram, Professor Henry I. Smith

The magnetic information storage density of hard drives has increased at the amazing rate of 60% per year for the last eight years. This growth is being achieved through evolutionary means involving scaling and improvement in all components of a hard drive: the head design, the signal processing, the media, etc. However, as the bits in the conventional thin film medium continue to decrease in size, thermal energy threatens to switch the individual grains that make up the bit, resulting in a loss of signal. There is wide agreement that a storage medium based on discrete, single-domain particles with uniform magnetization (Figure 26) may be scaled two orders-of-magnitude beyond the physical limits of conventional media.

We have initiated a program to develop fabrication techniques to generate high-density arrays of magnetic nano-particles and investigate their applicability to data storage. Our goal is to explore the effects of particle size, shape, inter-particle spacing, and material composition on magnetization reversal, thermal stability, and particle interactions; and to realize the necessary densities via fabrication techniques that are compatible with low-cost manufacturing. To the latter end, we take advantage of the high resolution capabilities of our interferometric lithography systems to define the two-dimensional pattern for such particles. To determine the effect of physical parameters such as particle size, shape, and material composition, we have developed process sequences for the fabrication of particles that fit into three general categories (Figure 25a) particles formed by electrodeposition, (b) particles formed by evaporation, and (c) particles formed by etching.

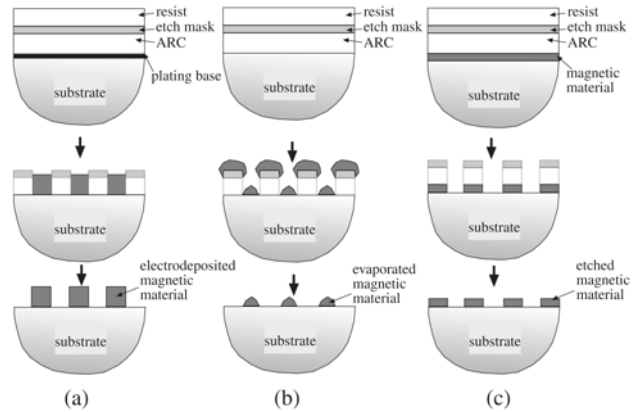


Figure 25. Schematic of three process sequences developed for the investigation of magnetic nano-particles with a variety of physical parameters. Lithographic exposure is by interferometric lithography or achromatic interferometric lithography. The antireflection coating (ARC) prevents backreflections from the substrate from interfering with the lithography. Sequence (a) illustrates the process of fabricating high aspect ratio magnetic pillars via electroplating. Sequence (b) involves the deposition of magnetic pyramids via evaporation and lift-off. Sequence (c) is appropriate for patterning magnetic islands in predeposited thin films.

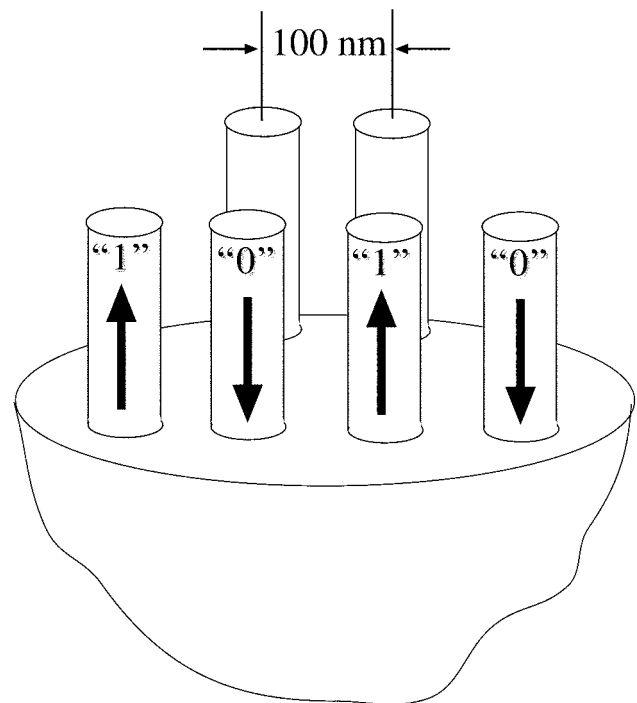


Figure 26. Schematic of high density magnetic information storage based on sub-100 nm sized magnetic particles.

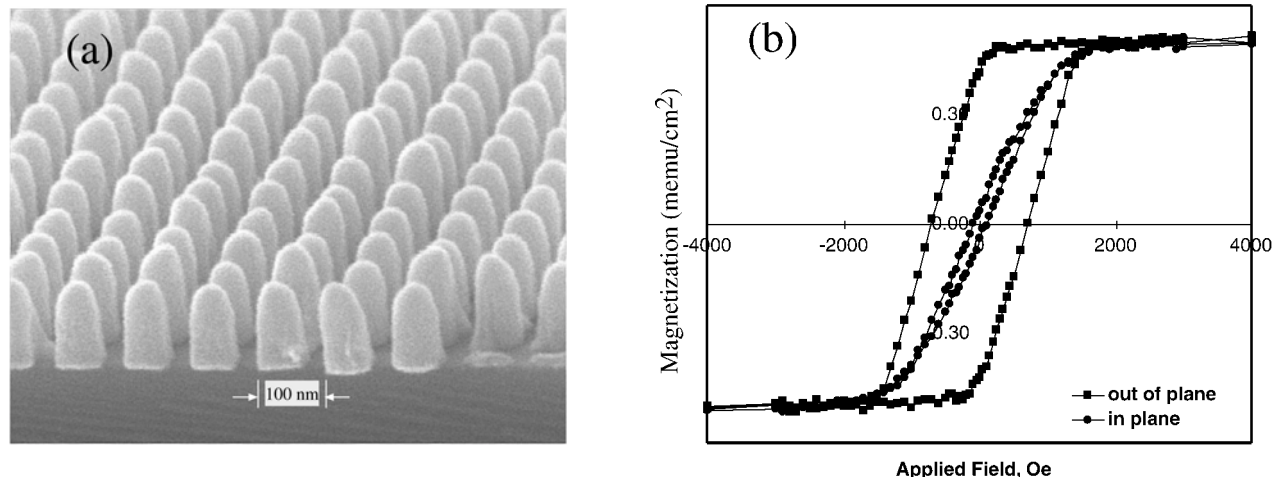


Figure 27. (a) Electron micrograph of 100 nm-period Ni pillars after the removal of the ARC plating template. (b) Plot of the magnetization of the pillars versus a magnetic field applied in-plane (dots) and out-of-plane (squares). The large magnetization at remanence (applied field = 0) for the out-of-plane compared to the in-plane applied field indicates that out-of-plane magnetization is favored.

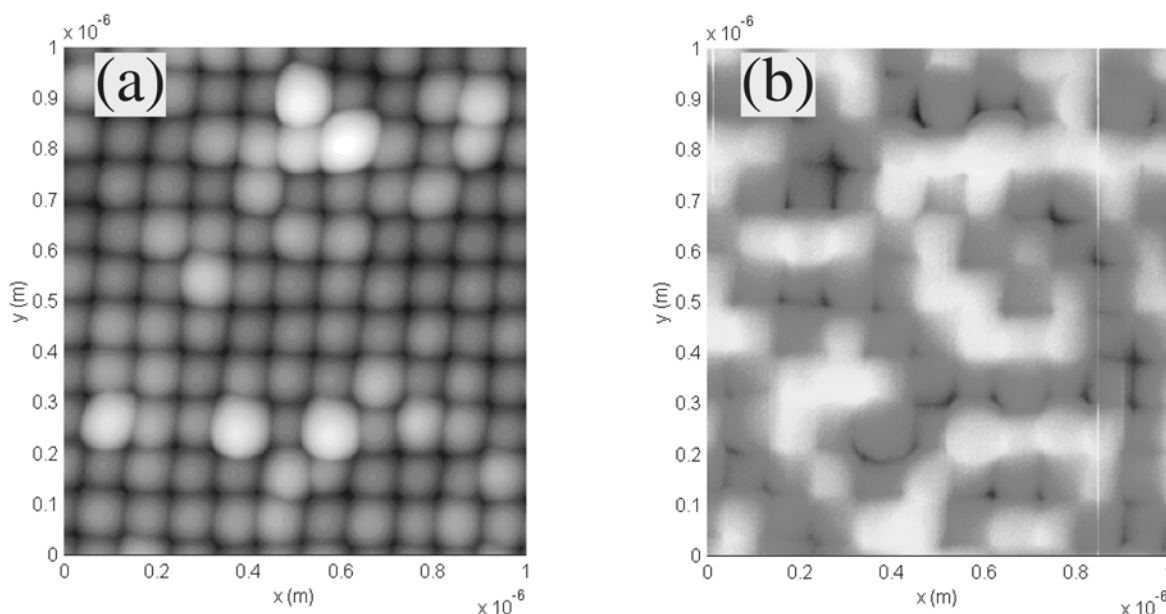


Figure 28. (a) Topography plot of the electroplated Ni pillars obtained by scanning the pillars with the tip of a magnetic force microscope and recording tip deflections. (b) Corresponding magnetic-force plot, where the light regions indicate "up" magnetization and the dark regions indicate "down" magnetization.

Electrodeposition involves forming a pattern of holes in a photoresist and transferring this pattern into an antireflection coating (ARC) polymer plating template. This method allows us to form high-aspect-ratio structures and thus to study the effect of shape anisotropy on magnetic behavior.

Figure 27a is a scanning electron micrograph of 100 nm-period, electrodeposited Ni pillars. The magnetization curves obtained by vibrating-sample magne-

tometry (Figure 27b) suggest that the pillars favor out-of-plane magnetization. Magnetic force microscopy performed on these pillars (Figure 28b) confirms perpendicular magnetization as illustrated in Figure 26. With a switching field of 700 Oe, these particles may be well suited for data storage. The second process sequence (Figure 25b) entails the evaporation of pyramids of ferromagnet into holes in a polymer, followed by liftoff of the template. Evaporated Ni pyramids of 100 nm-period (Figure 29a) are

small enough to exhibit unstable magnetization at room temperature. However, at 10 K, they too favor out-of-plane magnetization (Figure 29b). The third process (Figure 25c) allows us to pattern thin films that have properties desirable for data storage. Using ARC posts as an etch mask and ion milling as an etching technique, one can pattern a thin film into islands of magnetic material, as shown in Figure 30.

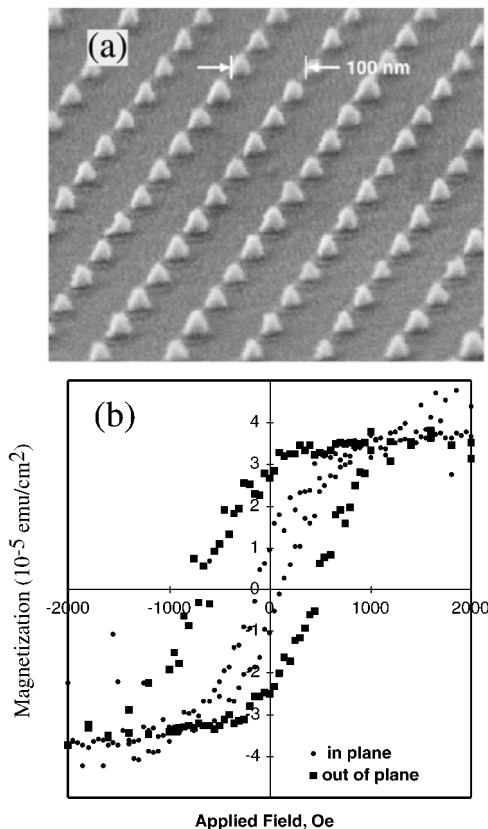


Figure 29. (a) Evaporated NiCr pyramids after lift-off. (b) In-plane (dots) and out-of-plane (squares) magnetization curves obtained by superconducting quantum interference device (SQUID) magnetometry at 10 K of a similar Ni sample. Such pyramids, whose magnetization is unstable at room temperature, also favor out-of-plane magnetization at 10 K.

In addition to patterned media, structures such as Figure 30 also have applications in magnetic random access memory (MRAM) devices. In an MRAM, data are stored into, and read from small magnetic particles using the magnetoresistive effect, in which the resistance of the magnetic particle depends on its magnetization state. We are etching spin valve multilayer magnetic stacks into dots to evaluate their magnetoresistive properties.

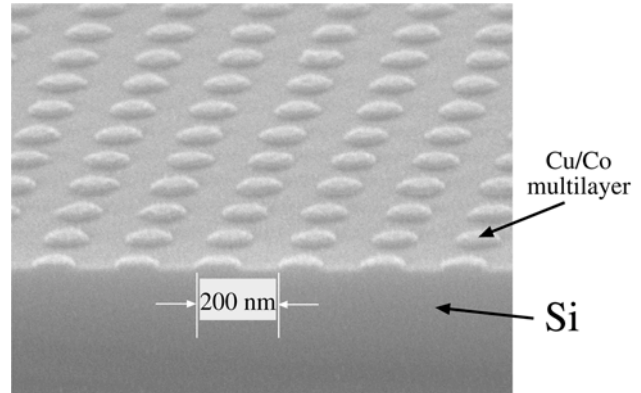


Figure 30. 200 nm-period islands of Cu/Co multilayers, patterned by interferometric lithography and ion milling, are suitable for magnetic random access memory (MRAM) applications.

3.11 Design and Fabrication of Single-Mask 50 nm MOSFETs

Sponsor

Defense Advanced Research Projects Agency/
U.S. Navy - Office of Naval Research
Contract N6601-97-1-8909

Project Staff

Keith M. Jackson, Zachary K. Lee, Professor Dimitri A. Antoniadis, Professor Henry I. Smith

As MOSFET dimensions are scaled to lengths below 100 nm, significant challenges arise in controlling fabrication processes. Rapid turnaround between process changes and device results, and an ability to extract the exact structure and doping of the fabricated device are tools critical to the development. The first requires a short-flow process that focuses only on the fabrication steps that critically define device performance in a minimum number of steps. The second tool, known as inverse modeling, couples a device simulator with an optimizing routine that shifts the doping in the simulated device until the current-voltage and capacitance characteristics of the simulated device match those of the real device. This project focuses on creating a short-flow process for 50 nm channel-length MOSFETs and coupling it with currently existing inverse modeling capabilities.

The short-flow process we have conceived will allow working MOSFETs to be fabricated in one mask step. It is shortened from a normal full-length MOSFET process by eliminating the need for oxide isolation around the devices and by eliminating the need for

the passivation and metal layers at the end of the process. Two types of structures will allow operational MOSFETs to be fabricated without field-oxide isolation. The first is an annular device where the source is completely enclosed inside of a gate and the drain is outside of the annular gate. The second structure is a figure-eight configuration (Figure 31) where the parasitic out-of-channel (i.e., field region) source-to-drain current is less than 0.02 times the in-channel current under the gate in the center of the structure. By using a self-aligned cobalt-silicide process (salicide), the source and drain will be low enough in resistivity that they can be contacted directly by probes. Even though two significant steps of the conventional fabrication process are left out, the steps that define the device operation—the gate stack, implantation, and critical high-temperature steps—are all contained in the short-flow process.

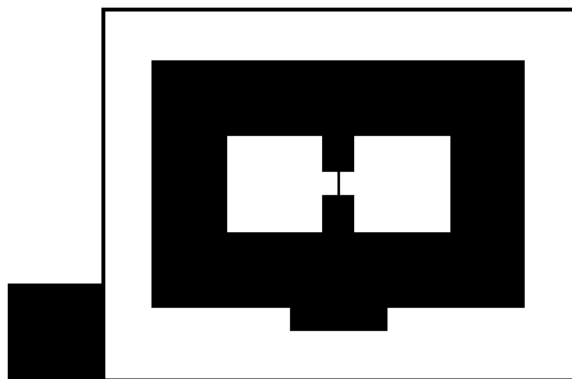


Figure 31. Gate mask layout of a figure-eight geometry MOSFET. The inner two white square areas are the source and drain probe pads that will be salicided. The dark wide ring is the gate pad with the active gate being the fine line in the center. The outer ring is a guard ring.

The gate-level lithography (the only lithography step) for the short-flow process will be done using x-ray lithography, easily allowing linewidths down to 50 nm. The mask will be fabricated with a mix of optical steps for the large features and e-beam writing for the fine gates. Using optically placed e-beam registration marks, the e-beam tool can match the in-plane scale and distortion of the optical projection tool to achieve good pattern placement.

The key elements in the fabrication of sub-100 nm devices are the placement of dopants and the use of very thin gate oxides. The accomplishments on the project this year have been in establishing process steps for these two key elements. NMOS and PMOS capacitors and long-channel MOSFETs with 20 Å

gate oxides have been fabricated and show low defect densities. They have active gate dopings around $4 \times 10^{19} \text{ cm}^{-3}$ at the polysilicon/oxide interface with minimal Boron penetration in the PMOS. A combination of low energy implants (1 - 2 keV Boron for the PMOS) and short, well-controlled thermal cycles (5 sec. or less at 1000° C) have allowed us to achieve source and drain depths of less than 10 nm for both NMOS and PMOS. These junctions have near ideal forward bias characteristics and have very low leakage in reverse bias. Having developed working processes for these device elements, the next set of devices will focus on optimizing the design of the ~30 nm deep source and drain extensions and the placement of counter-doping as halos or pockets around these junctions.

Once devices are fabricated using the short-flow process, their doping and structural components can be evaluated via inverse-modeling, using current-voltage and capacitance measurements. Understanding what doping profiles were achieved versus the original design then will allow us to go back and adjust the process and to see how changes affect the doping profiles in the device. This approach should facilitate the optimization of device fabrication for deep-sub-100 nm MOSFETs.

3.12 CMOS Technology for 25 nm Channel Length

Sponsors

Defense Advanced Research Projects Agency/
U.S. Navy –Office of Naval Research
Grant N66001-97-1-8909

Project Staff

Anthony J. Lochtefeld, Mitchell W. Meinhold, Iliia Sokolinski, Professor Dimitri A. Antoniadis, Professor James Chung, Professor Henry I. Smith

The scaling of CMOS transistors into the deep sub-100 nm region is extremely challenging because of short-channel effects. We are pursuing two distinct approaches that should permit scaling to 25 nm channel lengths. Both can be considered three-dimensional-gate CMOS (3-DG-CMOS) technologies. One is a planar twin-gate configuration, with either joint or independent control of the two gates per MOSFET; the other features a gate that surrounds a pillar-like vertical channel.

Monte-Carlo modelling predicts that twin-gated devices that are scaled to $L_{\text{eff}} = 25\text{nm}$ will have transconductances G_m in excess of $2000\text{ mS}/\mu\text{m}$, while maintaining almost perfect sub-threshold slope. However, models also predict that the tolerance in aligning front and back gates has to be within $L_g/4$ in order to avoid performance deterioration due to overlap capacitance. The $L_g/4$ requirement translates into 6 nm alignment tolerance for a 25 nm channel. In order to meet this alignment challenge we will use the IBBI alignment technique which achieves sub-nanometer misalignment detectivity. The planar twin-gate devices will be fabricated starting with a SIMOX wafer. First the gate stack for the back-gate will be deposited and patterned by x-ray lithography. The structure will then be covered by a layer of CVD oxide, planarized, and bonded to a "handle wafer." The bulk of the SIMOX wafer will then be chemically etched using the back-oxide of the SIMOX wafer as the etch-stop. The fabrication will then follow a conventional SOI process, with front gate precisely aligned to back-gate layer using the IBBI alignment scheme. The final structure is depicted in Figure 32.

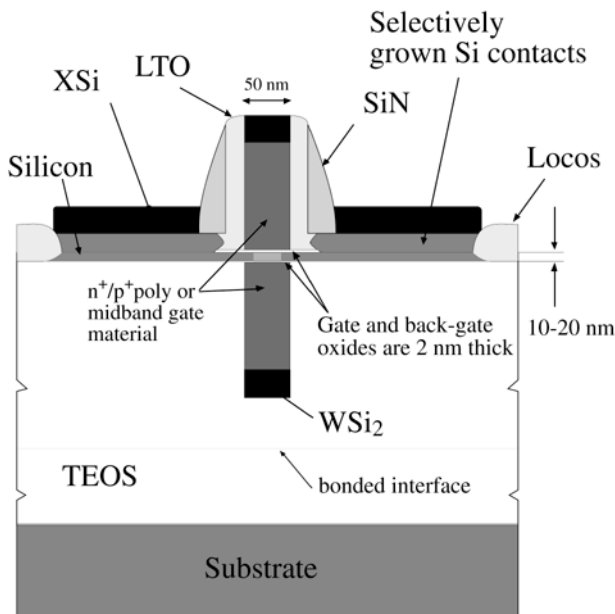


Figure 32. Dual gate n-MOS transistor with 25 nm effective channel length.

For gate-to-gate alignment, it is necessary to detect poly-Si alignment marks beneath the single-crystal-Si channel layer. We have demonstrated IBBI signal detectivity of such alignment marks buried beneath 100nm of amorphous Si, which has greater absorption than single-crystal-Si.

The second approach to 3-DG-CMOS utilizes epitaxially grown vertical pillars of Si. Such a structure addresses two major problems in ultrashort-channel MOS fabrication. First, a surround-gate has maximum possible control of the channel potential, improving sub-threshold slope and reducing short-channel effects to allow scaling of the effective channel length (L_{eff}) down to 25 nm for pillar MOS device $40\text{-}50\text{ nm}$ in diameter. Second, epitaxial definition of a vertical channel allows almost arbitrarily short L_{eff} with tighter control than is possible with current lithography technologies. In planar MOS devices, gate length is limited by lithography; the inherent variability in the lithography and etch processes can lead to unacceptable variation in L_{eff} from device to device and wafer to wafer. This is especially critical in ultrashort-channel devices, where the threshold voltage is extremely sensitive to gate length.

Previously demonstrated processes for epitaxially-defined vertical MOS structures generally start with the etching of a pillar from the epi wafer and suffer from severe difficulties in the subsequent contact and isolation of gate and source/drain regions. These problems are avoided in our proposed vertical-MOS process, illustrated in Figure 33, where the gate electrode material and dielectrics for source/drain isolation are deposited prior to hole-definition and epitaxial growth.

We are currently experimenting with selective epitaxial growth in features down to 100 nm in diameter in oxide on silicon, a key technology for our novel vertical-MOS process.

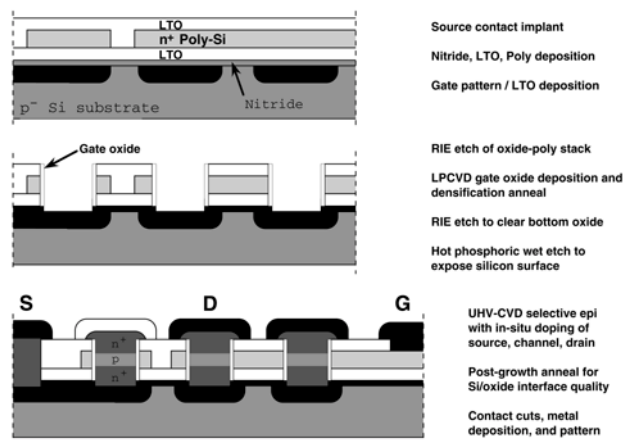


Figure 33. Process for fabricating surround-gate vertical MOS devices.

3.13 Deep-Ultraviolet Contact Photolithography

Sponsor

Defense Advanced Research Projects Agency/
U.S. Navy - Naval Command, Control,
and Ocean Surveillance Center
Grant N66001-98-1-8921

Project Staff

James M. Daley, Mark K. Mondol, Dr. James G. Goodberlet, Professor Henry I. Smith

A research program in deep-ultraviolet contact photolithography was begun this year. The goal of this project is to demonstrate a lithography process capable of patterning sub-100 nm features at high rates ($> 3 \text{ cm}^2/\text{sec}$) on spherical surfaces (radius of curvature as low as 8 cm). The lithography scheme must also be amenable to precise multilevel alignment, i.e., subsequently patterned levels must be aligned to previous levels to within a small fraction of the minimum feature size. A successful lithography scheme which meets these criteria will be used to fabricate a smart, wide-field-of-view camera. This camera will have detectors and high-speed signal-processing hardware on its curved focal plane. We believe that contact photolithography best fulfills these requirements.

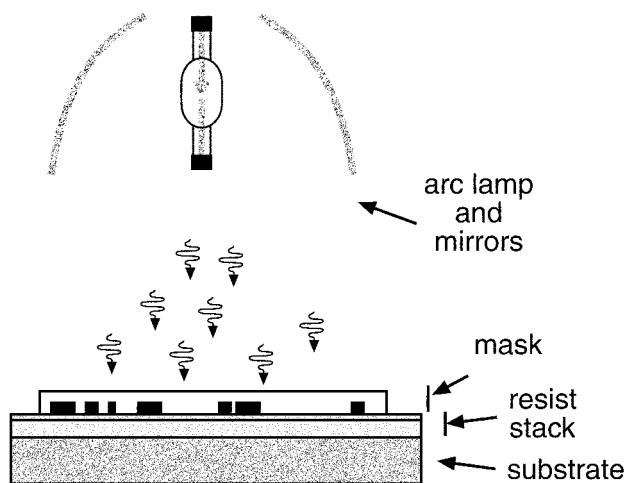


Figure 34. Deep-ultraviolet contact photolithography is a simple exposure process in which the mask, with patterned absorber, and resist-coated substrate are brought into intimate contact. In our experiments, the wavelength of the exposing radiation is as short as 220 nm and comes from a Hg(Xe) arc lamp.

The basic approach of contact photolithography is depicted in Figure 34. An optically-transparent mask with a patterned absorber is brought into contact with a resist-coated substrate and then exposed with radiation. After exposure, the resist is developed to provide the desired relief pattern. This method was developed earlier for patterning electrodes on surface-acoustic wave devices, which typically had expensive and unconventional substrates. Our initial tasks are to extend the resolution of contact photolithography down to the sub-100 nm regime and then pattern on doubly-curved surfaces. To pattern on the curved surface we plan to use very thin, i.e., 1 to 10 μm thick, conformable membrane masks.

The practical resolution limit of the contact photolithography scheme is determined by the mask design and wavelength of the exposing radiation. We have considered three mask designs: (1) amplitude mask (AM), (2) embedded amplitude mask (EAM), and (3) embedded attenuating phase-shift mask (EAPSM). These designs are depicted in Figure 35. The amplitude mask is the easiest to fabricate, and we have done preliminary exposures with this type. The EAM and the EAPSM are designs which improve the resolution of the lithography by taking advantage of the high refractive index of the mask substrate. This is because the optical mode which traverses the region between absorbers can be confined more tightly in the high-refractive index material and propagate normally rather than decay evanescently. With these masks, the minimum printable feature size is approximately $\lambda/(2n)$, where n is the refractive index of the mask substrate.

For the EAPSM, the absorber transmits about 18% of the incident radiation and imparts a π phase shift to it. This design suppresses undesirable lateral-diffraction. Both the embedded mask designs may be covered with a thin protective layer which will facilitate mask cleaning and assist in minimizing any problems due to particles. Particles are highly problematic for contact photolithography because our modeling indicates that for sub-100 nm features, gaps between mask and substrate greater than 20 nm cannot be tolerated. With an exposing wavelength of 220 nm and either the EAM or EAPSM, we expect to print ~ 70 nm features with broad process latitude.

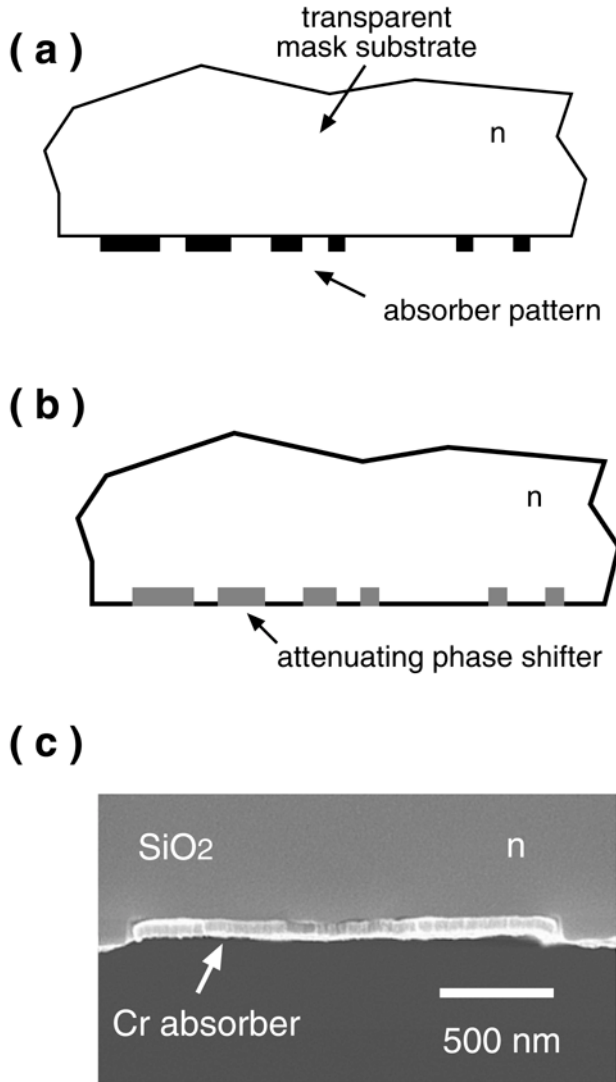


Figure 35. Close-up views of three mask designs are shown. Details of the patterned region of the amplitude mask (AM) (a) and of the embedded attenuating phase-shift mask (EAPSM) (b) are illustrated. The EAPSM suppresses undesirable diffraction effects. A third mask design, the embedded amplitude mask (EAM), has been fabricated, as shown by the SEM image in (c), and is similar to the EAPSM. The EAPSM and EAM improve the resolution of the lithography scheme by taking advantage of the mask substrate's high refractive index, n .

To measure the resolution limit of deep-ultraviolet contact photolithography, we have conducted several preliminary experiments with 150 μm -thick quartz amplitude masks. In one set of experiments, radiation from a Hg lamp ($\lambda \sim 365 \text{ nm}$) was used for exposures. In another experiment, a wavelength of 220 nm from a Hg(Xe) lamp was used. Figure 36 shows features patterned via contact photolithography. The first pattern consists of nested Λ 's exposed in 60 nm-thick photoresist. The fidelity of the printed pattern is

good and shows no line shortening or corner distortions. The linewidths of the Λ 's are about 145 nm, and the exposure rate was 10 cm^2/sec . Isolated lines of 100 nm width were produced with the 220-nm exposure, but at a much slower rate because of the weak Hg(Xe) lamp and a slow-speed resist. (With the use of a commercial short-wavelength laser, the exposure rate could be increased to more than 3 cm^2/sec .) After development, gold was electroplated into the mold formed by the resist. These results give us high confidence that sub-100-nm features can be patterned with deep-ultraviolet contact photolithography using the EAM or EAPSM.

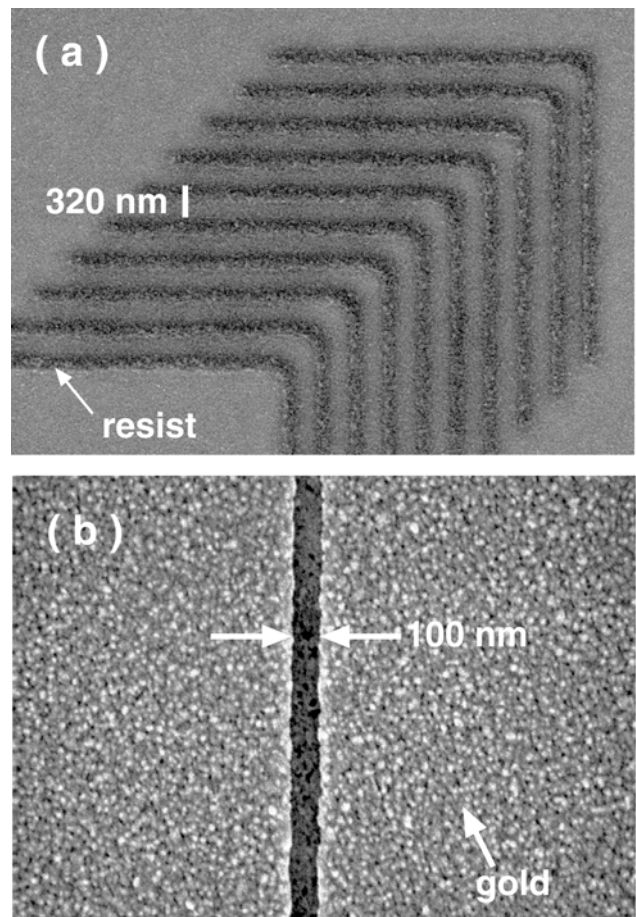


Figure 36. These patterns were made with amplitude masks and contact photolithography. In (a), nested L's were patterned in 60-nm-thick photoresist with an exposing wavelength of 365 nm. In (b), 100-nm-wide isolated lines were patterned with an exposing wavelength of 220 nm, and after development, gold was electroplated into the mold formed by resist.

In subsequent experiments, we will compare the resolution-limit of the different mask designs and evaluate process latitude for each. We will also test multi-level alignment.

3.14 Fabrication of Three-Dimensional Photonic Bandgap Structures

Sponsor

National Science Foundation
Grant DMR 98- 08941

Project Staff

Minghao Qi, Professor John D. Joannopoulos, Professor Henry I. Smith

Three-dimensional photonic bandgap structures (PBG) are true optical analogs of semiconductors in a sense that they present omni-directional bandgaps for photons. Figure 37 illustrates the 3-D structure we are attempting to fabricate using planar fabrication techniques. Modeling indicates that it has a large, complete bandgap, which allows defects to be introduced in a controlled manner.

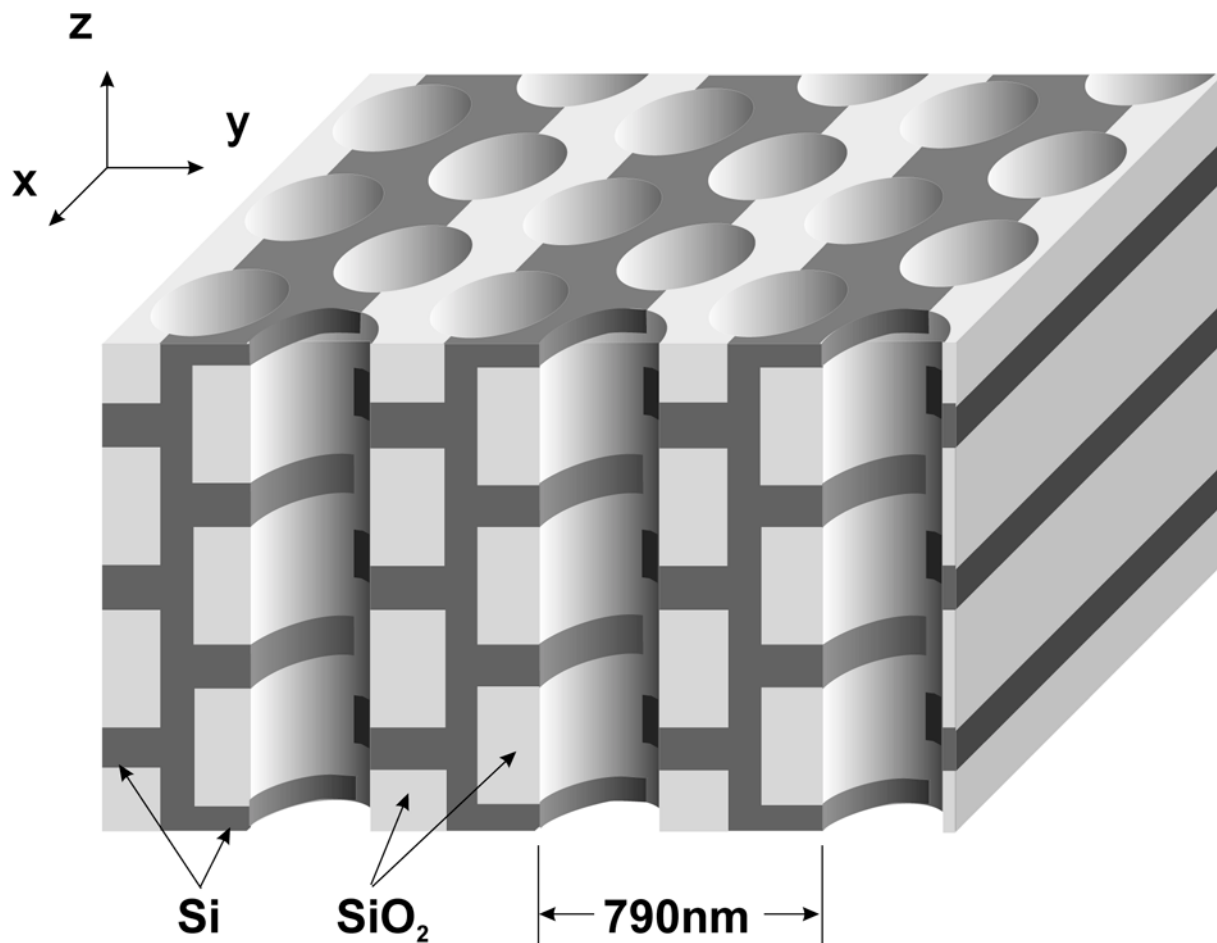


Figure 37. Depiction of a 3D photonic-bandgap (PBG) crystal to be fabricated at a 790 nm period. The dark gray and light gray regions correspond to Si, with a high index (3.4), and SiO₂, with low index (1.4), respectively. The SiO₂ can be removed after the structure is formed, and that will increase the ideal bandgap from 14% to 21% of the midgap frequency, which corresponds to a wavelength of 1.53 μm. The design enables planar fabrication techniques to be applied.

Figure 38 illustrates the completion of the first two layers of the structure. The amorphous silicon layers are sputter deposited at room temperature, and the patterns are aligned and defined using our VS2A scanning-electron-beam lithography (SEBL). The misalignment is shown to be within 45 nm, which is sufficient to support the upper layer structures. Then SiO₂ is conformally deposited via high-density

plasma-enhanced CVD at 80° C, which also provides planarization. The etch back of the SiO₂ to the level of the Si is done by a combination of controlled dry etching with CHF₃/O₂ and wet etching with diluted HF. This approach should be extendable to five to seven layers, which are required to achieve the true 3-D bandgap.

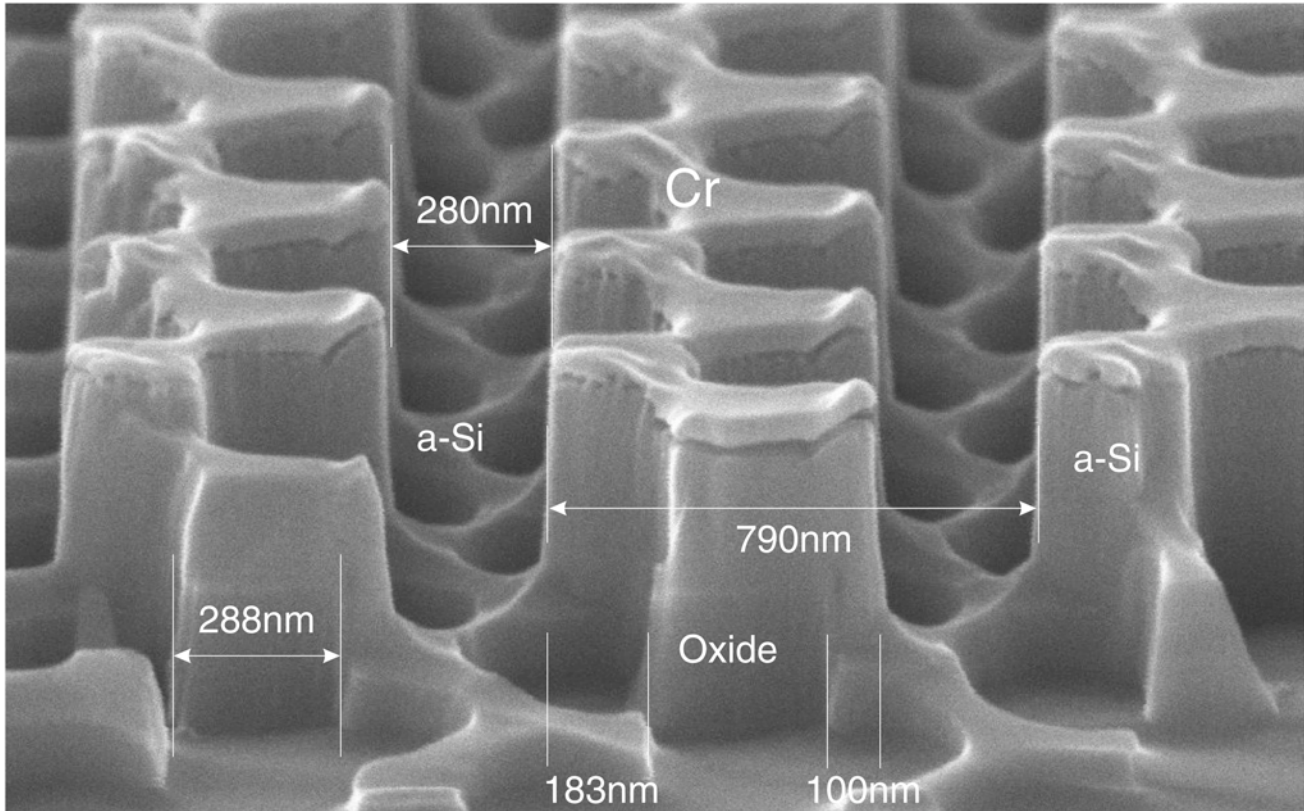


Figure 38. Scanning-electron micrograph of the patterned second layer of a 3-D photonic-bandgap structure, showing amorphous Si on top of the first-layer structure, with grooves filled with SiO_2 . The second layer structure is shifted by half of the periods in both x and y directions. An intentional overetch into the first layer is also observable.

3.15 Fabrication and Design of an Integrated Channel-Dropping Filter in InP

Sponsor

U.S. Air Force - Office of Scientific Research
Grant F49620-96-1-0126

Project Staff

Juan Ferrera, Jeffrey T. Hastings, M. Jalal Khan, Elisabeth M. Koontz, Michael H. Lim, Thomas E. Murphy, Dr. Jay N. Damask, Professor Leslie A. Kolodziejski, Professor Henry I. Smith

Wavelength-division multiplexing (WDM) is a strategy for utilizing the enormous bandwidth capacity of optical communications systems by multiplexing many data signals, each placed at a different wavelength. In order to realize the full potential of WDM, narrow-band filters are needed to differentiate between the many wavelength channels of interest.

The channel-dropping filter (CDF) is a critical component for such WDM systems. The function of the CDF is to drop (or add) one wavelength channel from a multi-channel bus. The key advantage of the CDF approach over many currently employed technologies is that one wavelength channel may be accessed without disturbing any of the remaining channels and without ever converting the data into an electronic signal. Thus, it offers a flexible and extendable means of all-optical routing.

Although it is widely recognized that WDM will play an increasingly important role in future communications systems, the fabrication of integrated optical components needed for WDM presents some unique challenges that have not been fully appreciated or adequately addressed. In this project, we demonstrate a novel process for fabricating integrated grating-based optical devices, which addresses some of these unique challenges.

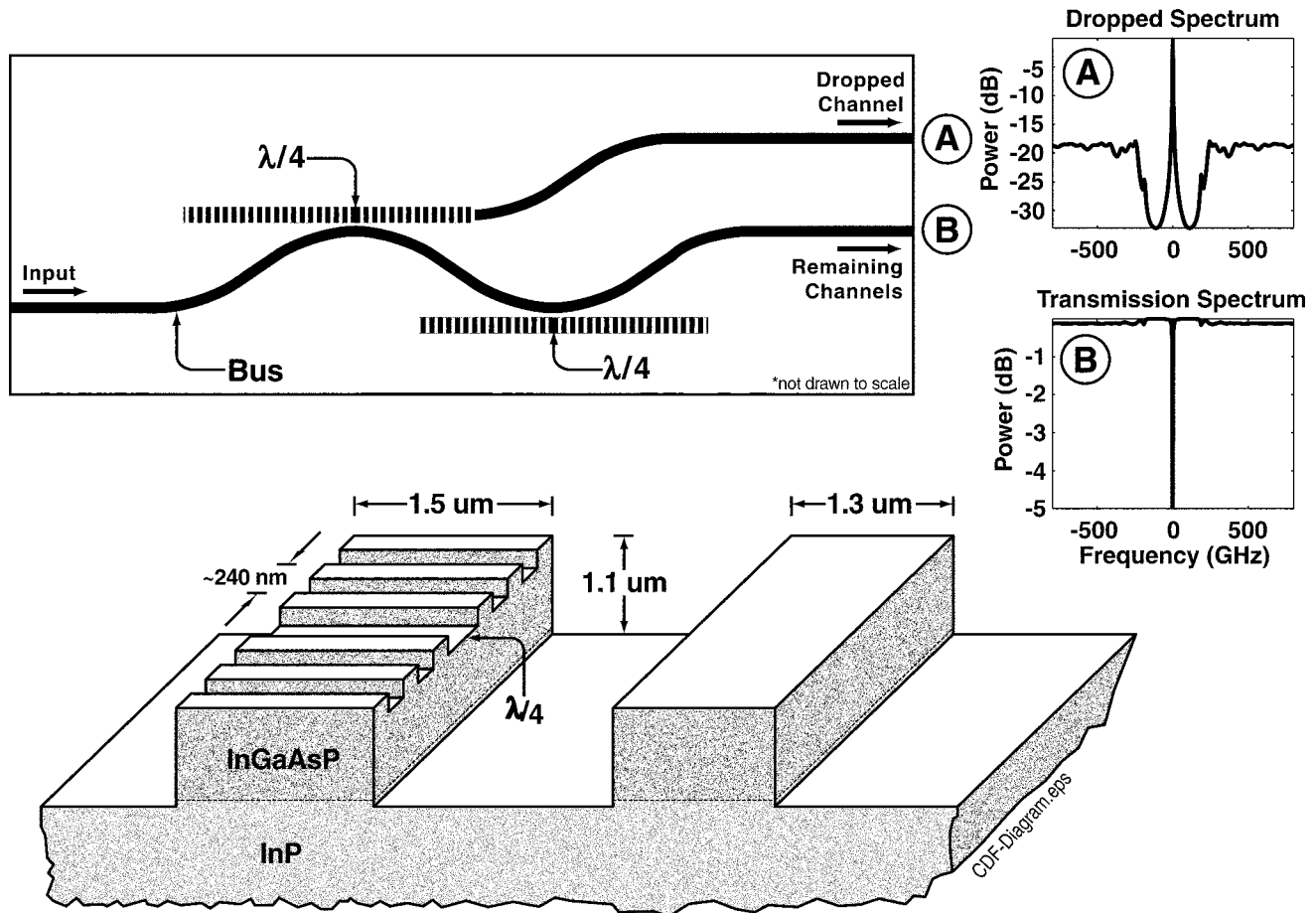


Figure 39. Diagram of the channel-dropping filter. As depicted in the upper portion, a multi-wavelength input signal is launched along the bus waveguide. One resonant wavelength-channel is dropped in the upper port of the device. As shown in the lower portion of the Figure, the waveguide is composed of InGaAsP, surrounded by an InP cladding. Note: the final top layer of InP is not depicted.

Figure 39 depicts the channel-dropping filter (CDF) which we are in the process of building in the Nanostructures Laboratory. The filtering action takes place in the quarter-wave-shifted Bragg gratings located above and below the bus waveguide. These gratings act as narrow-band resonators, which are only excited by one resonant wavelength channel.

Some of the fabrication challenges presented by this device are: (1) a fine-pitch (244.4 nm) grating must be etched into the top of the much taller (1.2 μm) waveguide, and its period must be controlled to within 0.1 nm. (2) The k-vector of the grating must be aligned with the axis of the waveguide to within 1.7 milliradians; any misalignment greater than this will cause the mode to lose guidance and scatter excessively. (3) Abrupt quarter-wave phase shifts must be placed at specified locations in the grating. (4) The InP must be grown over the grating without altering the square-wave shape of the underlying quaternary.

To meet these requirements, we have developed a dual-hardmask process (DHP), depicted in Figure 40. This DHP enables us to avoid the difficult problem of lithographically patterning 0.1 micron features over extreme topography. We first lithographically define the grating in a hardmask, using x-ray lithography. We then deposit a second hardmask directly on top of the grating, and define the waveguide pattern in it using contact photolithography.

Once the two hardmasks are patterned, the waveguides and gratings are formed by a sequence of dry etching steps. The only constraint on the choice of hardmask materials is that the one on top can be removed without affecting the one below. We use Ni for the waveguide-level mask and Ti for the underlying grating-level mask. Figure 40 includes a micrograph of a structure fabricated using this process.

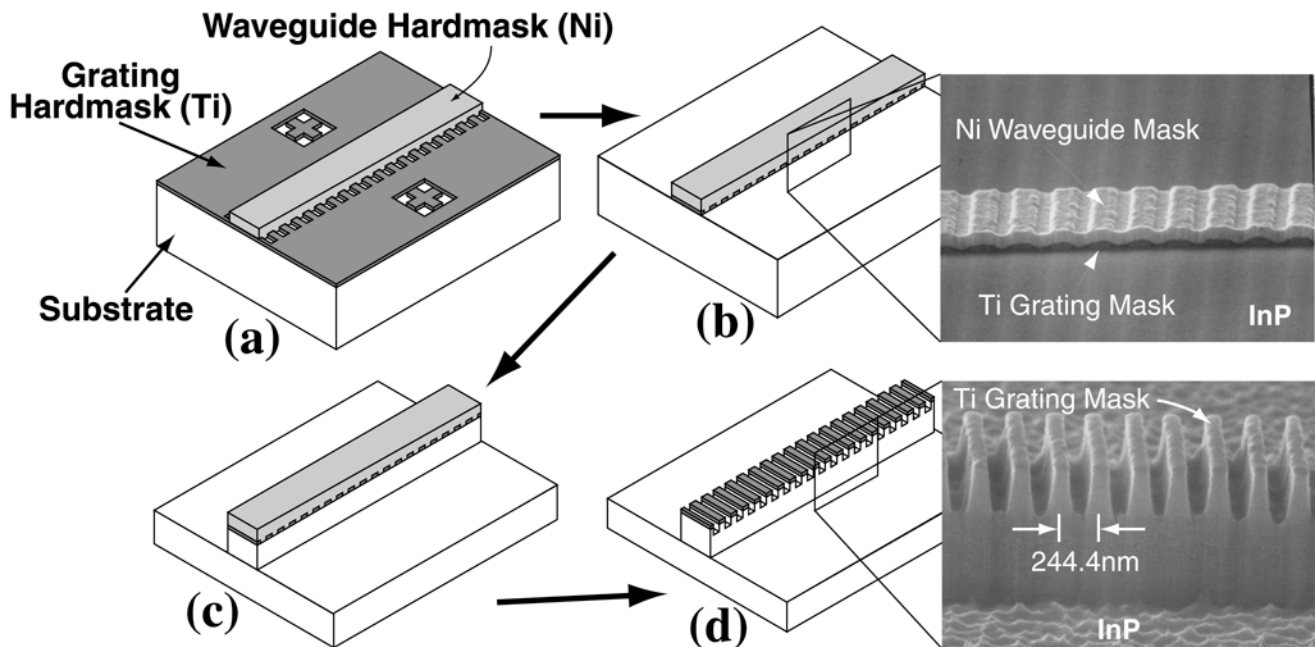


Figure 40. The dual-hardmask process (DHP) is used to pattern the fine-period gratings atop the InGaAsP waveguides. (a) First the grating-level hardmask is patterned over the substrate, then the waveguide-level mask is patterned over the grating-level mask.; (b) the excess grating mask is stripped; (c) the waveguide features are dry-etched; (d) after removal of the waveguide mask, the grating features are dry-etched.

The grating-level x-ray mask is written using a technique which we call spatially-phase-locked e-beam lithography (SPLEBL). In SPLEBL, interferometric lithography is first used to generate a coherent grating pattern on the x-ray mask. Then e-beam lithography is used to write the arbitrary patterns required by the device. During the e-beam writing, the interferometrically-generated grating pattern on the mask is sampled in order to determine the absolute beam position. This technique ensures that the e-beam writes a coherent grating, free of stitching errors.

The waveguide mask is written at a commercial mask supplier using a MEBES tool. Both the x-ray mask and the optical photomask have complementary alignment marks to enable angular alignment of the grating k-vector with the waveguide axis.

We believe that the fabrication techniques developed for this device will prove useful for constructing a variety of related, active and passive grating-based devices.

3.16 Fabrication of an Integrated-Optical Grating-Based Matched Filter for Fiber-Optic Communications

Sponsor

U.S. Air Force - Office of Scientific Research
Grant F49620-96-1-0126

Project Staff

Juan Ferrera, Michael H. Lim, Thomas E. Murphy,
Dr. Jay N. Damask, Professor Henry I. Smith

For future all-optical communications systems, filters are needed for a wide variety of network functions including dispersion-compensation, wavelength multiplexing, gain flattening, and noise suppression. This project seeks to develop the technology for building such filters, using integrated Bragg gratings. Integrated gratings provide a convenient way to perform filtering operations in a package that can be integrated on a chip, along with other electronic and optical components of the communications system.

Figure 41 depicts the structure of a novel integrated-optical filter we are developing in the Nanostructures Laboratory. The filtering action is performed by the shallow corrugation etched into the top surface of the Ge-doped silica waveguide. As depicted, the period of the grating is ~530 nm, which places the spectral response in the 1550 nm communications band. In order to separate the reflected filtered signal from the

incident input signal, a Mach-Zehnder interferometer is used. In this configuration, light is launched into the top waveguide and a codirectional coupler splits the signal between the upper and lower arms of the interferometer. The reflected signals are recombined in the coupling region and emerge in the lower port of the device.

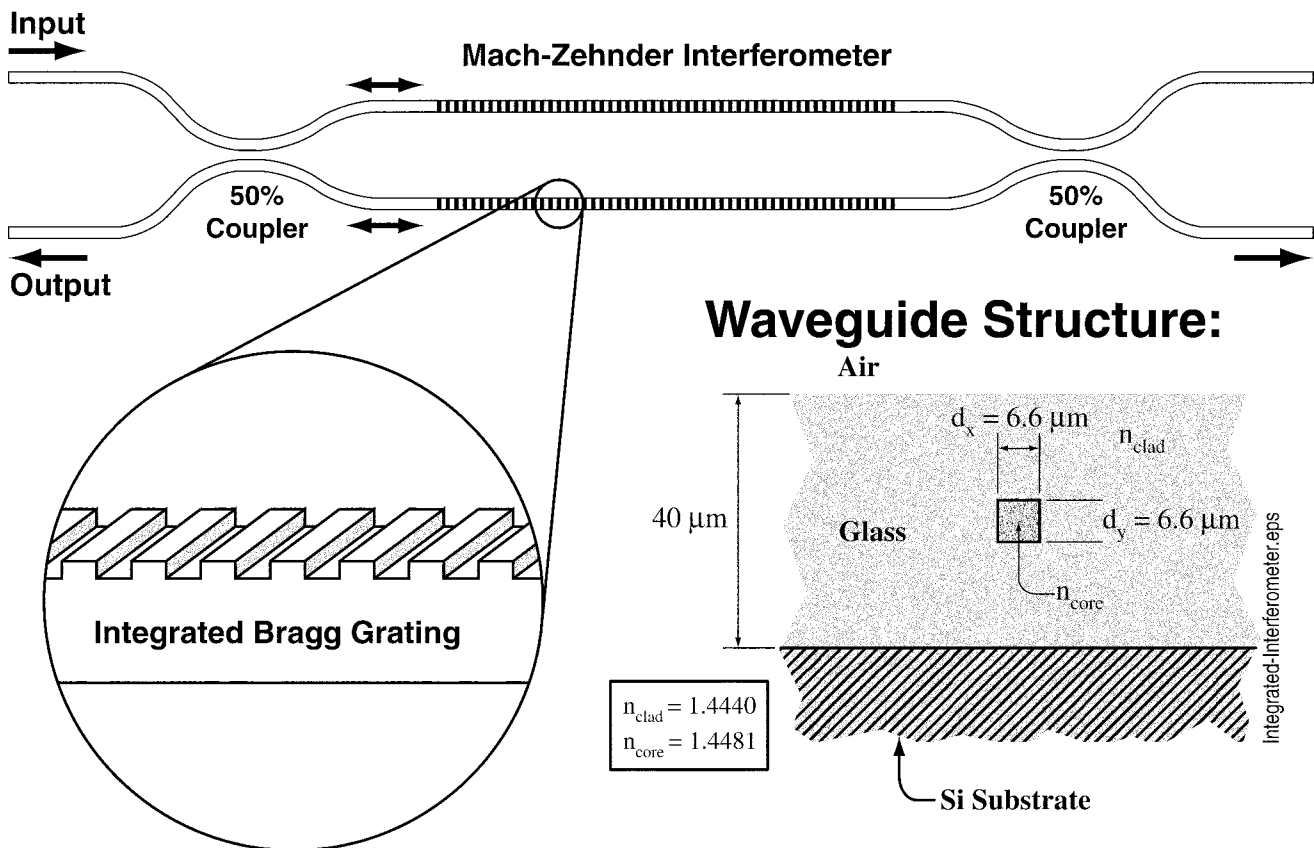


Figure 41. Diagram of an integrated optical matched-filter. The waveguide consists of a germanium-doped SiO₂ core, 6.6 μm wide and tall, surrounded by SiO₂ cladding. The 10 mm-long Bragg grating is formed by etching a shallow, 535 nm-period grating onto the top of the waveguide before the upper cladding layer is deposited. The waveguide interferometer is designed to redirect the reflected, filtered signal to a separate output port.

The spectral response of this device can be tailored by adjusting the geometry of the Bragg grating. For example, to achieve a notch-type filter with high out-of-band rejection, the grating amplitude can be apodized over the length of the device. To construct a grating filter for dispersion-compensation, the grating period could be gradually chirped over its length. In this project, our goal is to build a grating filter that has a spectral response that is matched to a communications signal of interest. The integrated Bragg-grating is an ideal filter for such an application, because if the length and shape of the grating are properly selected, the reflection spectral response of

the grating can be made to have a characteristic sinc shape which is matched to that of a binary communications signal.

Other laboratories are developing similar devices using fiber-Bragg-gratings. In such devices, the grating is formed via a UV-induced index change in the core of an optical fiber. Some researchers are attempting to construct integrated filters by applying the same UV-induced technique to a planar waveguide structure. Our work is unique in that the grating is formed by physically etching a corrugation onto the integrated waveguide structure. This

approach allows us to: (1) tailor the shape of the grating on an almost tooth-by-tooth basis, (2) take advantage of existing nanoalignment techniques to achieve accurate alignment of the grating to the waveguides without any kind of in-situ monitoring, and (3) circumvent the inherent limitations of photo-refractive gratings. For these reasons, we believe our approach is not only more flexible, but also more suitable for mass-production of highly integrated optics.

As described in our related article concerning the InP channel-dropping filter, we have developed a flexible and robust method of constructing integrated Bragg-grating-based devices which solves some of the critical problems of alignment, period selection and grating fidelity. This approach is also applied to these silica waveguide devices.

Our fabrication sequence uses photolithography to define the waveguide features of the device and a combination of interferometric lithography, e-beam lithography, and x-ray lithography to print the fine-period grating structures.

At present, we have fabricated and measured a set of preliminary waveguide-coupler devices. These initial devices, which do not have a corrugated grating on the top surface, allow us to measure the propagation loss, fiber-coupling loss, polarization dependence and waveguide-to-waveguide directional coupling. For these coupler devices, we measured a total insertion loss lower than 1 dB, which includes propagation loss, fiber-coupling loss, and bending loss. Having characterized the waveguide structure, we have now turned our attention to the Bragg grating. Our current efforts focus on investigating the overgrowth properties of silica cladding over fine-period grating structures.

3.17 High-Dispersion, High-Efficiency Transmission Gratings for Astrophysical X-ray Spectroscopy

Sponsor

National Aeronautics and Space Administration
Contract NAS8-38249

Project Staff

Robert C. Fleming, Patrick S. Hindle, Michael McGuirk, Edward R. Murphy, Dr. Mark L. Schattenburg, Professor Claude R. Canizares, Professor Henry I. Smith

Through a collaboration among the Center for Space Research (CSR), the Nanostructures Laboratory (NSL), and the Microsystems Technology Laboratories (MTL), x-ray transmission gratings are fabricated for the NASA Advanced X-ray Astrophysics Facility (AXAF) x-ray telescope, scheduled for launch on the Space Shuttle in 1999. This major national facility will provide high-resolution imaging and spectroscopy of x-ray-emitting astrophysical objects, with unprecedented power and clarity, promising to significantly widen our view of the Universe.

Many hundreds of large-area, gold transmission gratings, with 200 nm and 400 nm periods, are required for the high-energy-transmission-grating spectrometer (HETGS) on AXAF, which will provide high-resolution x-ray spectroscopy in the 100 eV to 10 keV band. In order to achieve spectrometer performance goals, the gratings need to have very low distortion (< 200 ppm), and high-aspect-ratio structures, significantly pushing the state-of-the-art of nanofabrication.

The need for high grating quality and an aggressive production schedule demanded the development of a robust, high-yield manufacturing process. We adopted a scheme involving interferometric lithography with tri-level resist, followed by cryogenic reactive-ion etching and gold electroplating (see Figure 42). A chemical etching step then yields membrane-supported gratings suitable for space use. The gratings underwent extensive testing before being assembled in the spectrometer.

A cleanroom fabrication facility was constructed (the Space Microstructures Laboratory, on the fourth floor of Building 37 adjacent to the Gordon Stanley Brown Building), in order to fabricate the AXAF gratings. The proximity of the lab to the MTL allowed the sharing of many services, such as DI and process water, nitrogen, process vacuum, and waste drains. The SML space includes 1700 sq-foot of Class 100 clean room and associated support areas and a large complement of state-of-the-art equipment.

Production of flight gratings and spares has been completed, and the fully assembled and calibrated HETGS flight instrument (see Figure 43) has been integrated with the AXAF spacecraft, which is now undergoing final test prior to launch.

AXAF Gold Transmission Grating

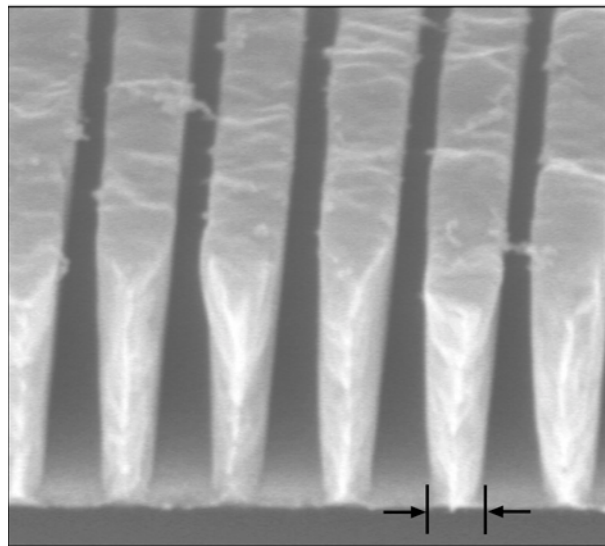


Figure 42. Scanning-electron micrograph of a 200 nm-period gold x-ray transmission grating, cleaved to show the sidewalls of 100 nm wide lines.

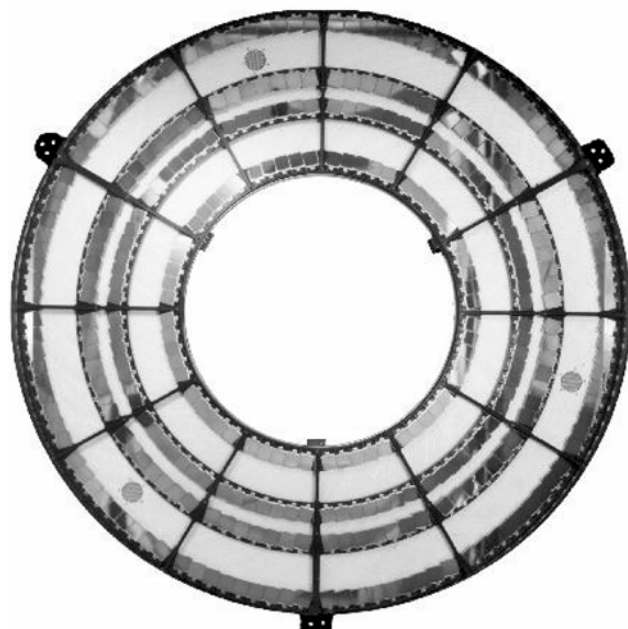


Figure 43. Photograph of the HETGS flight instrument, which consists a 1.0 meter-diameter aluminum wheel populated with hundreds of 200 nm and 400 nm-period gold x-ray transmission gratings (340 total).

3.18 Super-smooth X-ray Reflection Gratings

Sponsor

National Aeronautics and Space Administration
Grant NAG5-5105
Contract NAS5-98037

Project Staff

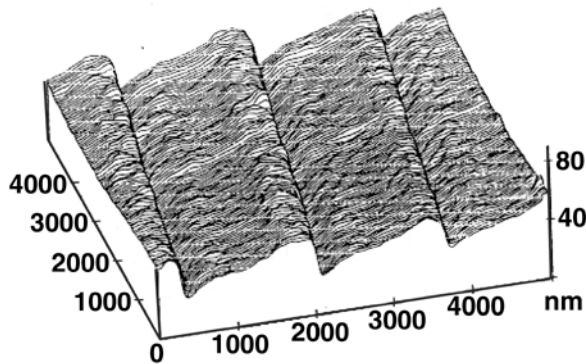
Carl G. Chen, Robert C. Fleming, Patrick S. Hindle, Michael McGuirk, Edward R. Murphy, Dr. Mark L. Schattenburg, Professor Claude R. Canizares, Professor Henry I. Smith

Grazing-incidence x-ray reflection gratings are an important component of modern high-resolution spectrometers and related x-ray optics. These have traditionally been fabricated by diamond scribing with a ruling engine or, more recently, by interferometric lithography followed by ion etching. These methods result in gratings which suffer from a number of deficiencies, including high surface roughness and poor groove profile control, leading to poor diffraction efficiency and large amounts of scattered light.

We are developing improved methods for fabricating blazed x-ray reflection gratings which utilize special (111) silicon wafers, cut ~ 1 degree off the (111) plane. Silicon anisotropic etching solutions, such as potassium hydroxide (KOH), etch (111) planes extremely slowly compared to other crystallographic planes, resulting in the desired super-smooth blaze surface. Previous work used similar off-cut (111) silicon substrates to fabricate blazed diffraction gratings. However, that method utilized a second KOH etch step which compromised the grating facet flatness and is unsuitable for small grazing-angle x-ray diffraction.

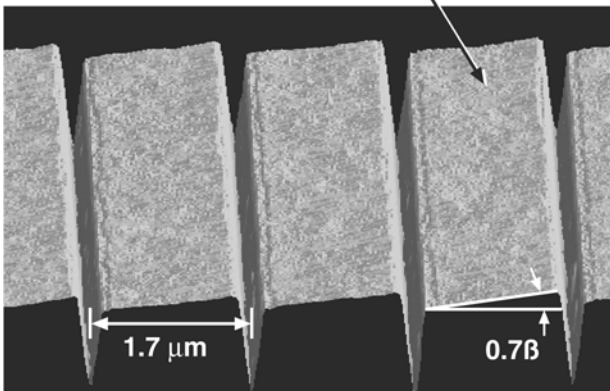
Our gratings are patterned using interferometric lithography with the 351.1 nm wavelength and transferred into the substrate using tri-level resist processing, reactive-ion etching (RIE), and silicon-nitride masking during the KOH etch. The narrow (~ 0.1 μm) ridge of silicon which supports the nitride mask is removed using a novel chromium lift-off step followed by a CF_4 RIE trench etch. The result is extremely-smooth sawtooth patterns, which, after applying a thin evaporative coating of Cr/Au, are suitable for x-ray reflection (see Figure 44). Gratings have been

tested with special x-ray spectrometers in the laboratories of our collaborators at Columbia University and the Lawrence Berkeley National Laboratory. Peak gratings efficiencies achieved are ~35% greater than those of the best available ruled masters of comparable design (see Figure 45).



(a) Mechanically Ruled

Si (111) planes,
<0.4 nm rms roughness



(b) Anisotropically Etched

Figure 44. (a) An AFM image of a traditional mechanically-ruled and replicated x-ray reflection grating.² Note the rough, wavy grating surfaces which lead to poor diffractive performance. (b) An AFM image of a blazed x-ray reflection grating fabricated by anisotropic etching of special off-cut (111) silicon wafers. Note the improvement of grating surface flatness and smoothness, leading to significantly improved performance.

Potential applications of these improved gratings are for laboratory and satellite-based high-resolution x-ray spectroscopy. The current phase of the work

involves patterning gratings on super-flat wafers and trimming the substrates into the desired rectangular format.

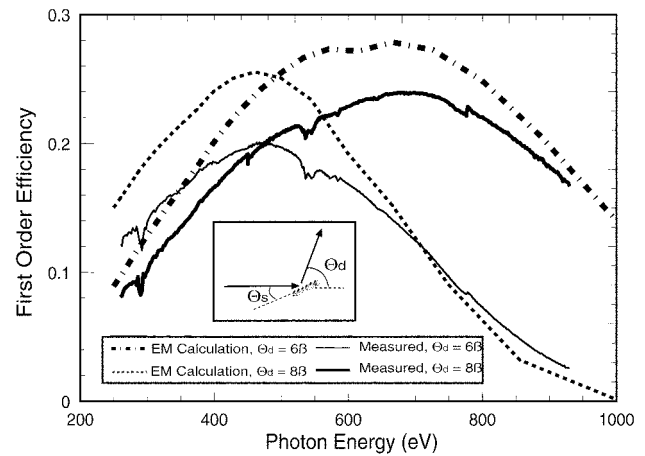


Figure 45. Comparison of x-ray diffraction efficiency measured at Lawrence Berkeley Laboratory and electromagnetic finite element calculations performed at Columbia University. Peak gratings efficiencies achieved are ~35% greater than those of the best available ruled masters of comparable design.

3.19 Transmission Gratings as UV-blocking Filters for Neutral Atom Imaging

Sponsors

Los Alamos National Laboratory

Contract E57800017-9G

Southwest Research Institute

Contract 83832

Project Staff

Robert C. Fleming, Patrick S. Hindle, Michael McGuirk, Edward R. Murphy, Dr. Mark L. Schattenburg, Professor Claude R. Canizares, Professor Henry I. Smith

Neutral-atom-beam imaging detectors are used to study dilute plasmas in laboratory systems such as Tokamaks, and in astrophysical environments such as the magnetospheric region of the Earth. Neutral atom emission can be a particularly useful probe of plasmas since neutrals travel in straight lines-of-sight, unperturbed by electromagnetic fields.

² J.V. Bixler, C.J. Hailey, C.W. Mauche, P.F. Teague, R.S. Thoe, S.M. Kahn, and F.B. Paerels, "Performance of a Variable-line-spaced Master Reflection Grating for Use in the Reflection Grating Spectrometer on the X-ray Multimirror Mission," *Proc. SPIE* 1549: 420-28 (1991).

Charge-exchange interactions between Solar-wind particles and atoms in the Earth's tenuous outer atmosphere are predicted to form strong currents of neutral atoms (mostly oxygen and helium) emanating from the Earth, which, if they could be imaged, would provide unprecedented real-time mapping of this complicated magnetohydrodynamic environment. This information would be valuable in order to safeguard the health of orbiting satellites and ensure the stability of our nation's electric power grid.

Unfortunately, sensitive orbiting neutral-beam detectors are easily overwhelmed by the bright flux of UV photons typically emitted from astrophysical plasmas (mostly the 121.6 nm emission from hydrogen and the 58.4 nm emission from helium). Filters which allow the passage of low-energy neutral atoms but block UV light are essential for the performance of this instrumentation. Through several years of collaboration with the Los Alamos National Laboratory (LANL), the University of West Virginia, the University of Southern California, and the Southwest Research Institute (SwRI), we have developed neutral beam filters which consist of mesh-supported, 200 nm-period, gold transmission gratings with 30-60 nm wide slots. The tall, narrow slots in the gratings behave as lossy waveguides at or below cutoff, providing UV discrimination on the order of millions.

We have been awarded contracts by LANL and SwRI to deliver a quantity of flight grating filters for the medium energy neutral atom (MENA) instrument on the NASA magnetospheric imaging medium-class explorer (IMAGE) mission, scheduled for launch in January 2000. We anticipate shortly a new LANL contract to fabricate improved gratings for the NASA two wide-angle imaging neutral-atom spectrometers (TWINS) mission.

The gratings are fabricated by interferometric lithography with tri-level resist, followed by cryogenic reactive-ion etching and gold electroplating. An additional masking step followed by nickel plating fabricates the mesh support structure, and a final chemical etching step yields mesh-supported gratings suitable for space use.

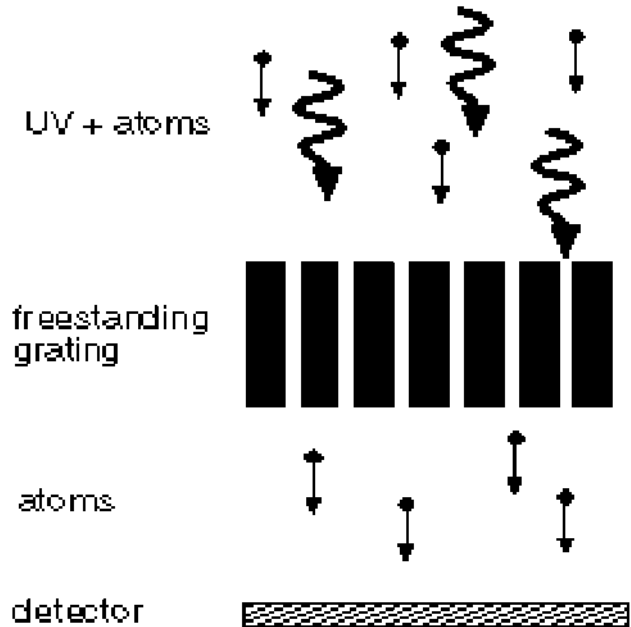


Figure 46. Concept of UV filtering by means of a metal freestanding grating. As a result of polarization and waveguide effects, UV is blocked while allowing the passage of atoms. In this way, UV background counts on the atom detector are avoided.

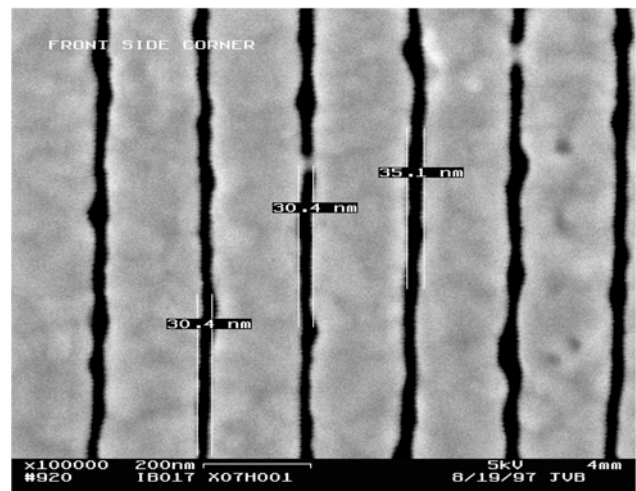


Figure 47. Scanning-electron micrograph image showing a close up of the UV blocking grating. Due to the narrow slot width of 30-35 nm, as shown in the picture, and the large slot depth (~500 nm), the UV transmission is extremely low (10^{-6} to 10^{-7} at 121.6 nm), while decreasing the transmitted atomic flux only by a factor of 10.

3.20 Submicron-Period Transmission Gratings for X-ray and Atom-Beam Spectroscopy and Interferometry

Sponsor

X-OPT, Inc.

Project Staff

James M. Carter, James M. Daley, Edward R. Murphy, Timothy A. Savas, Dr. Mark L. Schattenburg, Professor Henry I. Smith

Transmission gratings with periods of 100 to 1000 nm are finding increasing utility in applications such as x-ray, vacuum-ultraviolet, and atom-beam spectroscopy and interferometry. Over 30 laboratories around the world depend on MIT-supplied gratings in their work. For x-ray and VUV spectroscopy, gratings are made of gold and have periods of 100 to 1000 nm, and thicknesses ranging from 100 to 1000 nm. The gratings are most commonly used for spectroscopy of the x-ray emission from high-temperature plasmas. Transmission gratings are supported on thin (1 micron) polyimide membranes or made self-supporting ("free standing") by the addition of crossing struts (mesh). (For short x-ray wavelengths, membrane support is desired, while for the long wavelengths, a mesh support is preferred in order to increase efficiency.) Fabrication is performed by interferometric lithography combined with reactive-ion etching and electroplating. Progress in this area tends to focus on improving the yield and flexibility of the fabrication procedures.

Another application is the diffraction of neutral-atom and molecular beams by mesh supported gratings. Lithographic and etching procedures have been developed for fabricating free-standing gratings and grids in thin silicon nitride (SiN_x) membranes supported in a Si frame. Figure 48 shows a free-standing 100 nm period grating in 100 nm-thick silicon nitride. Figure 49 shows a 100 nm-period grid in a 100 nm-thick SiN_x membrane. Such a grid is used in experiments as a "molecular sieve."

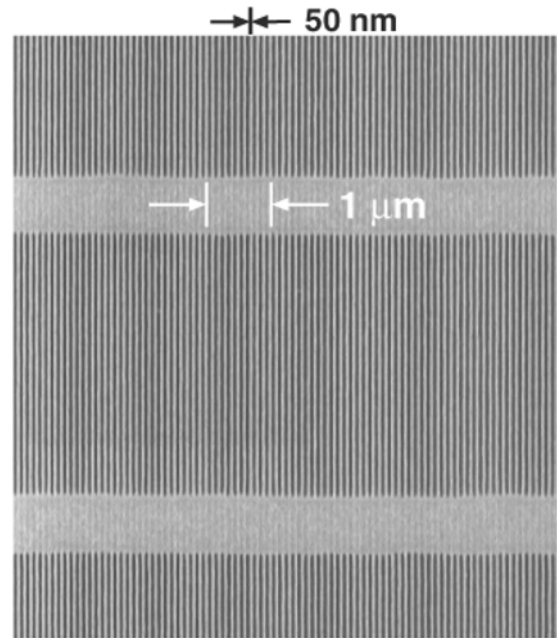


Figure 48. Scanning electron micrograph of a free-standing 100 nm-period grating (50 nm-wide bars) in a silicon nitride membrane of area 500 microns by 5 mm.

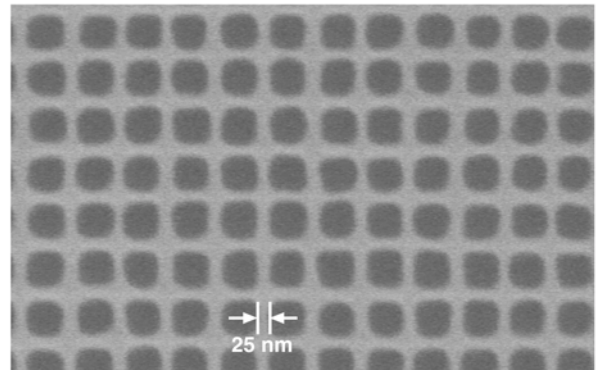


Figure 49. Scanning electron micrograph of a free-standing 100 nm period grid in a silicon nitride membrane of area 500 micron by 5 mm. Such grids are used in experiments to separate out Helium H_3^+ trimers from other clusters.

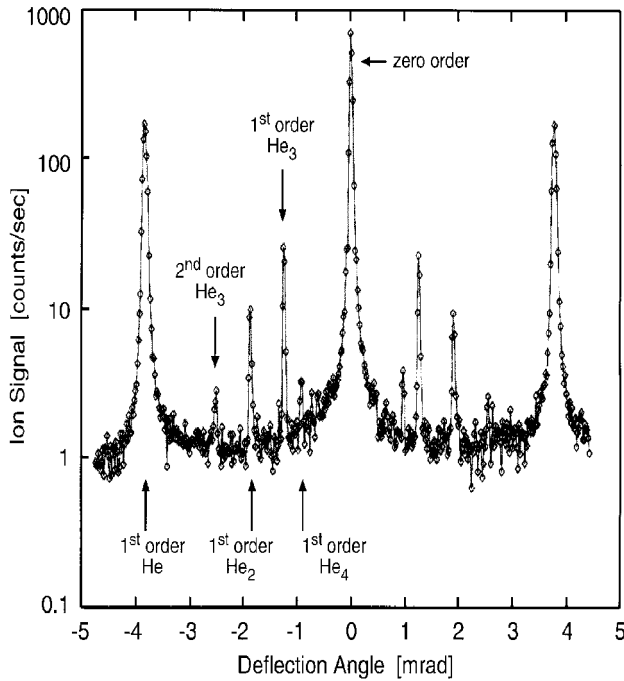


Figure 50. Helium beam diffraction spectrum. These results were obtained by Wieland Schoellkopf and Peter Toennies at the Max-Planck Institute in Goettingen, Germany, using a grating such as in Figure 54.

We have established a collaboration with the Max-Planck Institute in Goettingen, Germany, in which they utilize our gratings and grids of 100 nm period in diffraction experiments using He atom beams. Figure 50 shows a spectrum obtained by diffracting a He beam through a 100 nm-period transmission grating. Figure 51 shows the transmission of a grating as a function of helium-beam incident angles. Data obtained by He diffraction at large incident angles showed Lyman ghosts in the spectrum. This data led to the development of new fabrication techniques to improve the quality of the free-standing gratings in silicon nitride. Diffraction spectra from gratings made with the improved process show no Lyman ghosts, illustrating the important synergy between applications and nanofabrication.

In addition, we have established a collaboration with Professor David E. Pritchard at MIT. His group uses our 100 nm-period gratings in diffraction and interferometer experiments with neutral sodium atom beams.

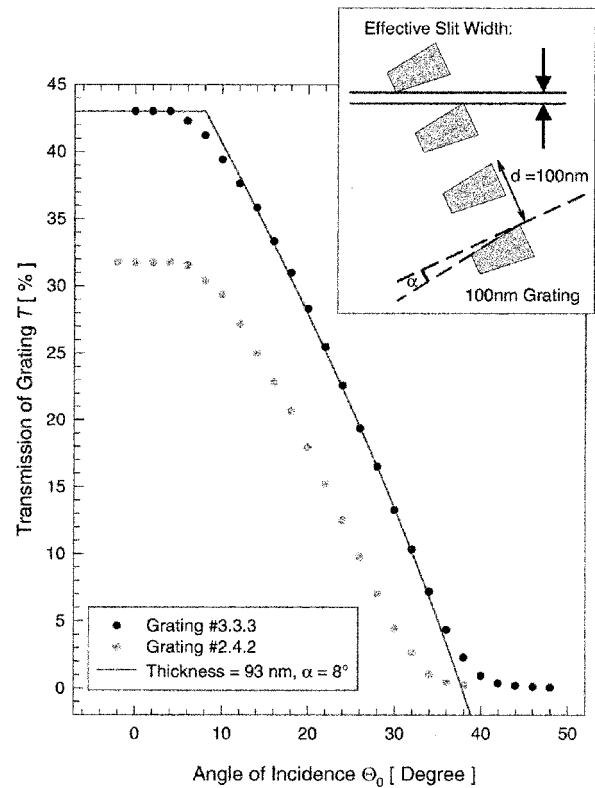


Figure 51. Measured total transmitted intensity through a 100 nm-period free-standing grating as a function of incident angle for a He atom beam. The line is a fit assuming a truncated wedge shape for the cross section of the grating bars, as depicted in the inset. Analysis indicated a grating thickness of 93 nm and a wedge angle of 8 degrees.

3.21 Sub-100 nm Metrology Using Interferometrically Produced Fiducial Grids

Sponsors

Defense Advanced Research Projects Agency/
U.S. Army Research Office
Grant DAAG55-98-1-0130

Project Staff

Carl G. Chen, Juan Ferrera, Paul T. Konkola, Dr. Mark L. Schattenburg, and Professor Henry I. Smith

The ability to see and measure the results of a process is critical to advancing fabrication technology. Historically, the development of improved microscopy techniques has led to rapid progress in microfabrication. Thus, the scanning-electron microscope was

essential to the microelectronics revolution. Similarly, the scanning-tunnelling microscope is creating a revolution in the study of interfaces and nanostructures.

In the past, metrology of microstructures and the measurement of workpiece distortion (e.g., a photolithographic reticle or an x-ray mask) has been based on point-by-point measurement through an optical microscope using an X-Y table monitored by a laser interferometer. Although this approach enables relative distances in a plane to be measured with 1 nm-level detectivity, it is expensive, tedious, and subject to a number of shortcomings, including the necessity of placing rather perturbative marks on a workpiece. We have initiated a new approach to metrology for the sub-100 nm domain that is based on large-area fiducial grids produced by interferometric lithography. This new approach is complementary to the point-by-point approach in much the same way that aerial photogrammetry is complementary to ground-based land surveying for the mapping of terrain.

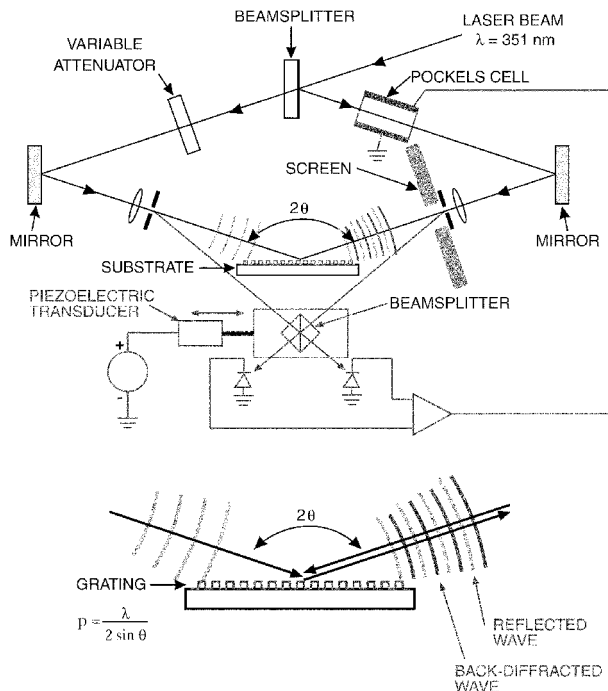
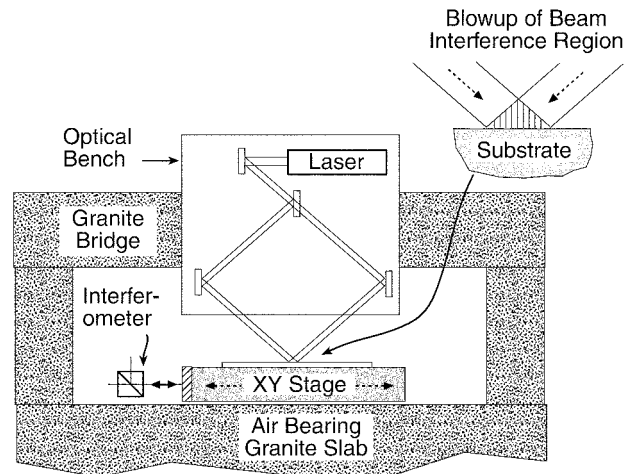


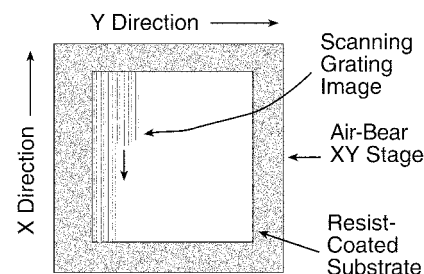
Figure 52. Schematic of the holographic phase-shifting interferometer (HPSI). A spherical wave back-diffracted from a shallow substrate grid, and a second wave specularly reflected, interfere on a fluorescent screen at the spatial filter. The fringes are imaged onto a CCD. By shifting the beam splitter with a piezo, a computer generates an X-Y map of phase error.

A key element in this new initiative is the holographic phase shifting interferometer (HPSI) interferometer, illustrated in Figure 52. This system, once it is fully

developed, will enable us to measure in a global manner the in-plane distortion of a workpiece, provided one of its surfaces contains a shallow fiducial grid. Ideally, the grid on the workpiece will be created by interferometric lithography or a derivative thereof, such as near-field holography.



a) Scanning beam interferometer.



b) Grating scanning method.

Figure 53. Schematic of the scanning beam interference lithography (SBIL) system. A pair of narrow, distortion-free beams overlap and interfere at the substrate, producing a small grating patch. The substrate is moved under the beams, writing a large area grating. Sophisticated electro-optical components (not shown) ensure phase locking of the grating during writing.

As part of this new initiative in sub-100 nm metrology, we are pursuing a variety of approaches to eliminating the distortion in interferometrically produced grids, decreasing the coefficient of the hyperbolic phase progression (a consequence of creating a grid by interfering spherical wavefronts), and increasing the useful area of fiducial grids. One such approach is scanning beam interferometric lithography (SBIL), depicted schematically in Figure 53. The concept here is to combine the sub-1 nm displacement measuring capability of laser interferometry with the inter-

ference of narrow coherent beams to produce coherent, large-area, linear gratings and grids. Our ultimate goal is to produce such gratings over areas many tens of centimeter in diameter.

3.22 Development of High-Speed DFB and DBR Semiconductor Lasers

Sponsor

MIT Lincoln Laboratory
Contract BX-6558

Project Staff

Farhan Rana, Michael H. Lim, Elisabeth M. Koontz, Professor Rajeev J. Ram, Professor Henry I. Smith, Professor Leslie A. Kolodziejski

High-speed semiconductor DFB and DBR lasers are crucial for high-speed optical communication links. These lasers can be directly modulated at frequencies reaching 20 to 30 GHz. They have important applications in optical links based upon wavelength division multiplexing (WDM) technology. Direct laser modulation schemes are much simpler to implement and integrate than modulation schemes based upon external modulators. However, modulation bandwidth of external modulators can easily go beyond 60 GHz. Thus, it is technologically important to have DFB/DBR lasers whose modulation bandwidths compete with those of external modulators. The goal of this project is to develop DFB and DBR lasers capable of being modulated at high speeds with low distortion and chirp.

High-performance DFB and DBR lasers demand that careful attention be paid to the design of the gratings, which provides the optical feedback. Spatial-hole burning, side-mode suppression, radiation loss, laser linewidth, spontaneous emission in nonlasing modes, lasing wavelength selection and tunability, laser-relaxation oscillation frequency etc. are all features that are very sensitive to the grating design. Improved grating design can significantly enhance laser performance, especially at higher modulation frequencies. In the last few years, various techniques have been developed in MIT Nanostructures Laboratory that allow fabrication of gratings with spatially varying characteristics and with long-range spatial-phase coherence.

Chirped optical gratings with spatially varying coupling parameter can be made using a combination of interferometric lithography, spatially phase-locked electron-beam lithography and X-ray lithography. This provides us a unique opportunity for exploring a wide variety of grating designs for semiconductor DFB and DBR lasers. We plan to explore laser devices suited for high speed as well as for low noise operation.

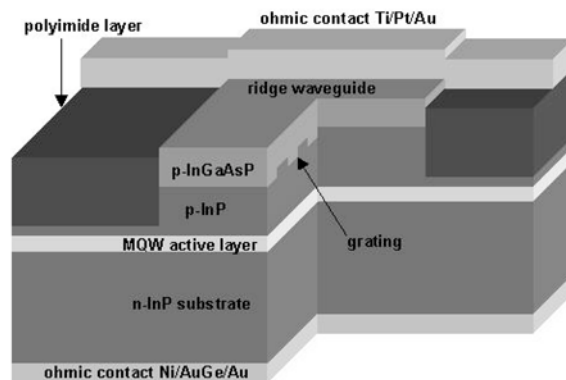


Figure 54. Schematic of a polyimide-planarized InP DFB ridge-waveguide laser.

We have developed techniques for fabricating high-speed, polyimide-planarized ridge waveguide laser structures that have low capacitance and are therefore ideally suited for high frequency operation. Figure 54 shows the cross section of a polyimide-planarized InP DFB laser. The active region consists of strain compensated InGaAsP multiple quantum wells. The grating and the ridge are dry etched in RIE using a mixture of hydrogen and methane. Planarization is achieved by spinning multiple coatings of polyimide followed by a high temperature cure. Cured polyimide is dry etched in RIE using a mixture of oxygen and carbon tetra-fluoride until the top of the ridge gets exposed. Ohmic contact to the ridge is made by lift-off on top of the polyimide layer. The thick layer of polyimide significantly reduces the capacitance between the top metal contact and the substrate. A large value of this capacitance can short out the active region at high frequencies. Figure 55 shows a scanning-electron micrograph (SEM) of a laser structure fabricated using this process.

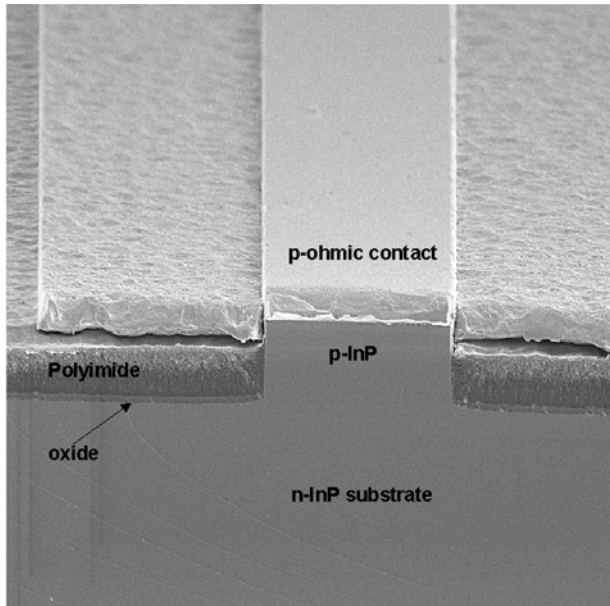


Figure 55. Scanning electron micrograph of a polyimide-palvanized InP ridge-waveguide laser.

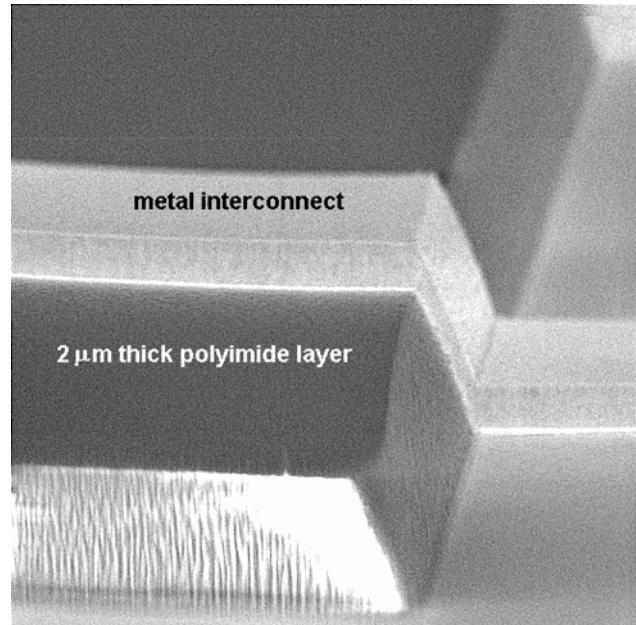


Figure 56. Scanning electron micrograph of a low capacitance polyimide based metal interconnect.

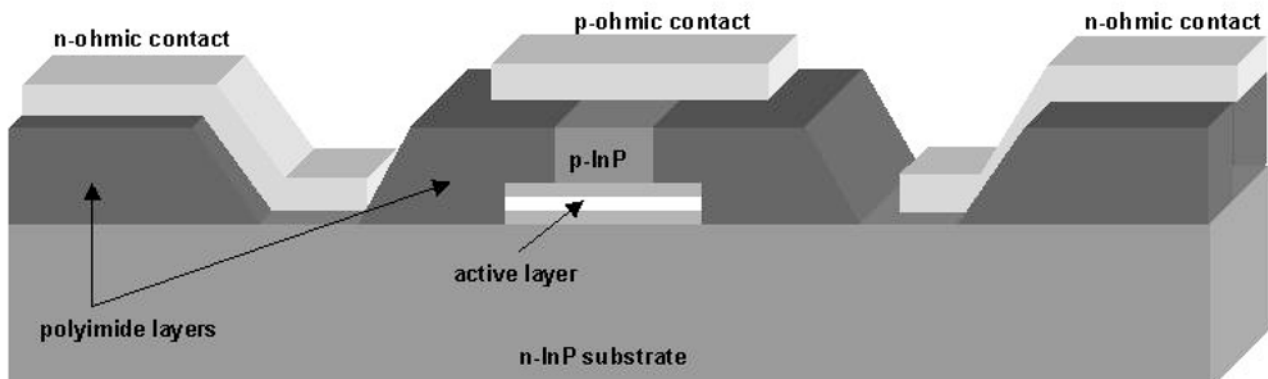


Figure 57. Co-planar stripline laser structure.

We are also developing techniques to fabricate co-planar stripline structures for high-speed DFB/DBR lasers. Co-planar striplines offer improved microwave performance compared to microstrip structures. Figure 57 shows a polyimide based co-planar stripline laser structure. Fabrication of this structure requires etching polyimide such that the sidewalls do not become too steep so that metal interconnects can be continuous over them. We have successfully developed etching techniques for polyimide that allows us to control the sidewall angle. Figure 56 shows SEM of a metal interconnect running over the sidewall of a polyimide layer.

3.23 Field Emitter Array Flat Panel Displays for Head-Mounted Applications

Sponsor

MIT Lincoln Laboratory
Contract BX-5956

Project Staff

David G. Pflug, Dr. Mark L. Schattenburg, Professor Akintunde I. Akinwande, Professor Henry I. Smith, Dr. Carl Bozler

Advances in nanostructure technology have made feasible small, high-resolution, high-brightness and high-luminous-efficiency field-emitter-array image sources for head-mounted displays (HMDs). HMDs are expected to have a variety of applications in military, medical, commercial and entertainment fields. The technology most commonly used in deployed HMD systems is the CRT which is bulky because of the use of a single electron gun to generate images on a cathodoluminescent screen but has the most desirable attributes of high luminous efficiency, high brightness and easy image rendition. However, the relay optics required for see-through HMDs become complicated because of the bulky nature of the CRT. For other applications, such as entertainment virtual reality, the most commonly used image source is the backlit active matrix liquid crystal display (AMLCD), which is thin and has high resolution. Furthermore, the addressing electronics are integrated on the same substrate as the image source. However, the backlit AMLCD image source does not have sufficient brightness nor luminous efficiency to make it suitable for application to see-through HMDs.

Our approach to demonstrating a small, high-resolution, high-luminous-efficiency and high-brightness display is the field-emitter-array flat-panel display (FED) which incorporates a high density, high performance array of low-voltage field emitters as shown in Figure 58. CMOS-controlled electron emission from the tips impinges on a cathodoluminescent screen. It is thus possible to integrate the addressing and signal conditioning electronics on the same substrate as the field emitter arrays (FEAs). The main advantage of this approach is the reduction of the number of wires and bond pads from about 2,000 to about 50. For example, it will be difficult to attach > 2,000 wires to bond pads in an area of 1.5 in \times 1.5 in and obtain ultra-high vacuum in the display envelope. High resolution (>1000 dpi) FEDs are only possible if the addressing/driver and other signal conditioning electronics are integrated on the same substrate as the field emitter arrays.

Our initial objective is to demonstrate the integration of Si CMOS technology with low-voltage field-emitter arrays fabricated using interferometric lithography. This project requires the fabrication of Si CMOS wafers with one or two levels of metal interconnect, followed by surface planarization using CMP technology. Interferometric lithography is then used to define Mo-cone field emitter arrays that are spaced 200 nm tip-to-tip and have <50 nm gate-to-emitter separation. Fabricated cone-field-emitter arrays with a 320

nm period have demonstrated emission currents of 1 mA at gate voltage of 20 V from 900 cones in a 10 μ m \times 10 μ m area. This current is more than adequate for a brightness of 1000 fL at a screen voltage of 500 V.

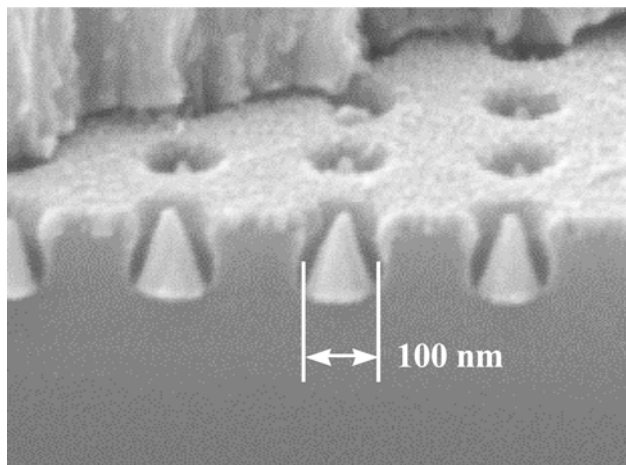


Figure 58. 100 nm gate aperture molybdenum field-emitter cones with chromium gate formed using a vertical evaporation.

Our initial efforts focused on modeling the scaling behavior of FEA devices. Numerical simulation and computer models to predict FEA performance have been developed and continue to be refined. These models allow us to obtain a correlation between different device geometries (cone tip radius or curvature, gate aperture, etc.) and the emitter's output characteristics. The results of this study have directed our fabrication efforts toward devices whose performance will not only be better, but more dependent on geometries that can be well controlled in the manufacturing process. Simulation results indicate that we will be able to increase the current density and reduce the operating voltage, by decreasing the tip-to-tip separation to 200 nm.

FEAs of 200 nm period have been fabricated using the interferometric lithography and integrated with additional metallization layers and conventional lithography to create discrete arrays for electrical characterization. The fabricated cones have similar size and structure to those simulated (Figure 58).

A semi-automated ultrahigh vacuum (UHV) probe chamber has been developed for the electrical characterization of FEAs. This test bed allows the performance of the arrays to be evaluated without the lengthy overhead of vacuum packaging devices. Device performance has been shown to be depen-

dent not only on the devices physical structure but also on surface contamination that may have resulted during fabrication and MEMS processing. The UHV probe chamber has the capability to do device conditioning including ECR plasma cleans and wafer bake-out. The system is designed to allow the future expansion to include surface analysis chambers including a kelvin probe, scanning maxwell microscope and auger.

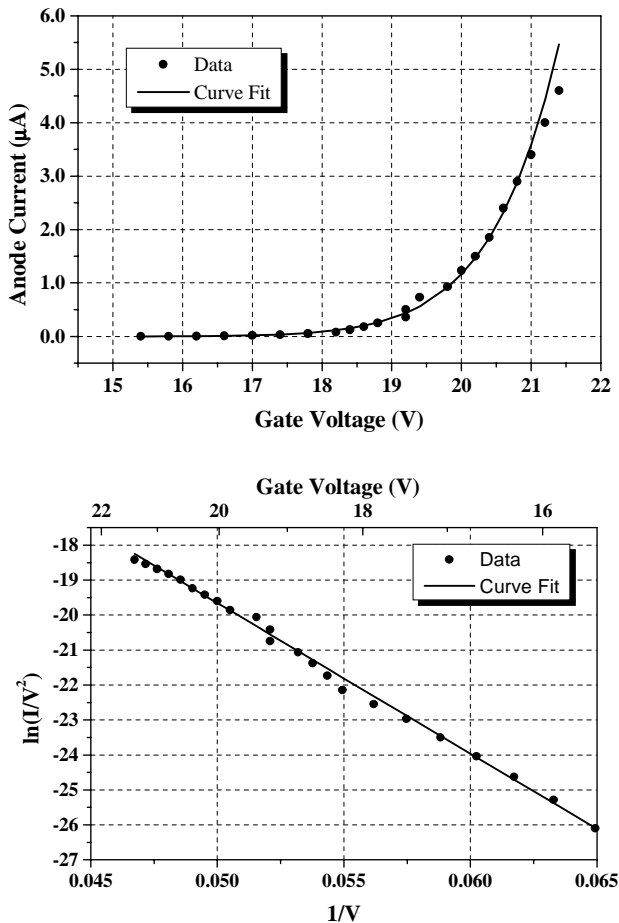


Figure 59. Anode current versus gate voltage for 100 nm gate aperture array. Fowler Nordheim plot confirming that field emission is the dominant contributing factor for the anode current.

Electrical characterization of the 100 nm aperture (200 nm tip to tip spacing) has shown that arrays can operate at voltages as low as 16 volts and provide adequate current to support flat panel display applications, as illustrated in Figure 59. We have demonstrated initial testing of low-gate-voltage FEAs with discrete solid state devices. We replace the resistor that previous approaches have used to limit and control emission current with a MOSFET. Current control is critical to the uniformity of brightness across the

display because Fowler-Nordheim emission depends exponentially on the ratio of the gate voltage to the tip radius-of-curvature (V_g/r). It is therefore very sensitive to small changes in the radius-of-curvature. It was possible to control the emitted current density using the gate voltage of the transistor load. This may enable analog voltage gray scale or temporal gray scale (Figure 60).

The above demonstration has gone a long way to show the feasibility of a high brightness, high-resolution FEA image sources for head-mounted displays.

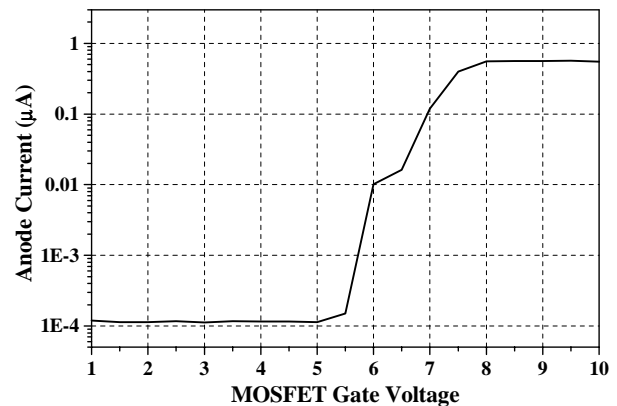


Figure 60. Array anode current versus MOSFET gate voltage showing control of over 3 orders of magnitude of the anode current with small variations in the MOSFET gate voltage.

3.24 Publications

Journal Articles

- Djomehri, I., T. Savas, and H.I. Smith. "Zone-Plate-Array Lithography in the Deep Ultraviolet." *J. Vac. Sci. Technol. B* 16(6): 3426-29 (1998).
- Goodberlet, J., J. Carter, and H.I. Smith. "A Scintillating Global-Fiducial Grid for Electron-Beam Lithography." *J. Vac. Sci. Technol. B* 16(6): 3672-75 (1998).
- Lim, K-Y., D.J. Ripin, G.S. Petrich, L.A. Kolodziejcki, E.P. Ippen, M. Mondol, H.I. Smith, P.R. Ville-neuve, S. Fan, and J.D. Joannopoulos. "Photonic Bandgap Waveguide Microcavities: Monorails and Air-bridges." *J. Vac. Sci. Technol. B*. Forthcoming. Paper presented at the 17th North American Conference on Molecular Beam Epitaxy, State College, Pennsylvania, October 4-7, 1998.
- Moon, E., J. Lee, P. Everett, and H.I. Smith. "Application of Interferometric Broadband Imaging Align-

- ment on an Experimental X-ray Stepper." *J. Vac. Sci. Technol. B* 16(6): 3631-36 (1998).
- Ross, C.A., and H.I. Smith. "Patterned Media: 200 Gb/in² or Bust." *Data Storage* 5(10): 41-48 (1998). (invited)
- Savas, T.A., M. Farhoud, M. Hwang, H.I. Smith, and C.A. Ross. "Properties of Large-area Nanomagnet Arrays with 100 nm Period Made by Interferometric Lithography." *J. Appl. Phys.* Forthcoming.
- Schollkopf, W., J.P. Toennies, T.A. Savas, and H.I. Smith. "A Cluster Size Nanofilter with Variable Openings between 2 and 50 nm." *J. Chem. Phys.* 109(21): 1-6 (1998).
- Twisselmann, D.J., M. Farhoud, H.I. Smith, and C.A. Ross. "In-Plane Magnetic Anisotropy in CoCrPt and CoCrTa Films Deposited onto Patterned Silicon Substrates." *J. Appl. Phys.* Forthcoming.
- U'Ren, G.D., M.S. Goorsky, E.M. Koontz, M.H. Lim, G.S. Petrich, L.A. Kolodziejski, V.V. Wong, H.I. Smith, K.M. Matney, and M. Wormington. "Analysis of Lattice Distortions in High Quality InGaAsP Epitaxial Overgrowth of Rectangular-Patterned InP Gratings." *J. Vac. Sci. Technol. B* 16(3): 1381-84 (1998).
- ### Meeting Papers
- Goodberlet, J., and H.I. Smith. "A Scintillating Global-Fiducial Grid for Electron-Beam Lithography." Paper presented at the 1998 Electron, Ion and Photon Beam Technology and Nanofabrication Conference, Chicago, Illinois, May 26-29, 1998.
- Goodberlet, J. "A Very-High-Density Scintillation-Data-Storage Device." Paper presented at the Conference on Micro and Nano Engineering, Leuven, Belgium, September 22-24, 1998.
- Koontz, E.M., G.D. U'Ren, M.H. Lim, L.A. Kolodziejski, M.S. Goorsky, G.S. Petrich, and H.I. Smith. "Overgrowth of (In,Ga)(As,P) on Rectangular-Patterned Surfaces Using Gas Source Molecular Beam Epitaxy." Submitted to *J. Crystal Growth* as part of proceedings paper for the 12th International Conference on Crystal Growth/10th International Conference on Vapor Growth and Epitaxy, Jerusalem, Israel, July 26-31, 1998.
- Pflug, D.G., M. Schattenburg, H.I. Smith, and A.I. Akinwande. "100nm Aperture Field Emitter Arrays for Low Voltage Applications." Paper published in the *Proceedings of the 1998 International Electron Devices Meeting*, San Francisco, California, December 6-9, 1998.
- Twisselmann, D.J., B.T. Adekor, M. Farhoud, H.I. Smith, P.C. Dorsey, and C.A. Ross. "In-Plane Anisotropy in CoCr(Ta,Pt)/Cr Films Deposited Onto Substrates With Controlled Topography." Paper published in the *Proceedings of the Materials Research Society 571*, San Francisco, California, April 13-17, 1998.
- Van Beek, J.T.M., R.C. Fleming, P.S. Hindle, J.D. Prentiss, and M.L. Schattenburg. "Nano-scale Freestanding Gratings for UV blocking Filters." *J. Vac. Sci. Technol. B* 16(6): 3911-16 (1998). Paper published in the *Proceedings of the 42nd International Conference on Electron, Ion, and Photon Beam Technology and Nanofabrication*, Chicago, Illinois, May 26-29, 1998.
- ### 3.24.1 Theses and Doctoral Dissertations
- Berman, D. *The Aluminum Single-Electron Transistor for Ultrasensitive Electrometry of Semiconductor Quantum-Confined Systems*. Ph.D. diss. Department of Electrical Engineering and Computer Science, MIT, June 1998.
- Carter, D.J.D. *Sub-50 nm X-ray Lithography with Application to a Coupled Quantum Dot Device*. Ph.D. diss. Department of Electrical Engineering and Computer Science, MIT, June 1998.
- Djomehri, I. *Zone-Plate-Array Lithography in the Deep UV*. S.M. thesis. Department of Electrical Engineering and Computer Science, MIT, September 1998.
- Moon, E. *Dynamic Nanometer Alignment for Nanofabrication and Metrology*. S.M. thesis. Department of Electrical Engineering and Computer Science, MIT, September 1998.
- Qi, M. *Micro-fabrication of 3-D Si/Air and Si/SiO₂/Air PBG Structures*. S.M. thesis. Department of Electrical Engineering and Computer Science, MIT, June 1998.